

**Transitional boundary layers caused by
free-stream turbulence**

by

Shahab Shahinfar

June 2011
Technical Reports from
Royal Institute of Technology
KTH Mechanics
SE-100 44 Stockholm, Sweden

Akademisk avhandling som med tillstånd av Kungliga Tekniska Högskolan i Stockholm framlägges till offentlig granskning för avläggande av teknologie licentiatexamen onsdagen den 9 juni 2011 kl 13:15 i sal S40, Teknikringen 8, Kungliga Tekniska Högskolan, Stockholm.

©Shahab Shahinfar 2011

Universitetsservice US-AB, Stockholm 2011

Shahab Shahinfar 2011, **Transitional boundary layers caused by free-stream turbulence**

Linné Flow Centre, KTH Mechanics, SE-100 44 Stockholm, Sweden

Abstract

The present measurement campaign on the free-stream turbulence (FST) induced boundary layer transition scenario has provided a unique set of experimental data, with potential to enhance the understanding of the effect of the free-stream turbulence characteristic length scales on the transition location and not only the turbulence intensity, which has been the focus in most previous studies. Recent investigations where the turbulence intensity has been kept essentially constant, while the integral length scale has been changed, show that the transition location is advanced for increasing length scale. However, the present data show that the integral and Taylor length scales of the FST have a relatively small influence on the transition location as compared to the turbulence intensity and data analyses are now directed towards enhanced understanding of how the different parts of the incoming energy spectrum affects the energy growth inside the boundary layer.

Preface

This licentiate thesis in fluid mechanics deals with boundary layer transition over a flat plate in presence of free-stream turbulence. The work is completely experimental. For this investigation, the hot-wire anemometry measurement technique, using two hot-wire probes, was used. The facility and methods are described in two chapters (2 and 3). Furthermore, the measurements were carried out in the streamwise, wall-normal and spanwise directions and the results are presented in three chapters 4, 5 and 6, respectively.

May 2011, Stockholm
Shahab Shahinfar

*Transition is a complex phenomenon, specially from Tradition
to Modernism.*

Anonymous

Contents

Abstract	iii
Preface	iv
Chapter 1. Introduction	1
Chapter 2. Experimental facility and measurement technique	4
2.1. The wind tunnel facility	4
2.2. Measurement technique	4
Chapter 3. Free-stream turbulence and base flow characteristics	8
3.1. Turbulence generating grids	8
3.2. Free-stream turbulence characteristics	12
3.3. Base flow characteristics	23
Chapter 4. Streamwise evolution of FST transitional boundary layer	29
4.1. Intermittency	29
4.2. Transition region	33
4.3. Streamwise evolution of second and higher order velocity moments	37
Chapter 5. Wall-normal profiles in transitional boundary layers	41
5.1. Streamwise evolution of mean velocity profiles	41
5.2. Integral quantities	42
5.3. Friction coefficient	43
5.4. Intermittency distribution in the wall-normal direction	44
5.5. Higher order velocity moments	47
5.6. Two-point correlation	50
5.7. Probability Density Function	54

Chapter 6. Spanwise measurements inside the transitional boundary layer	56
6.1. Mean velocity and the higher order moments including intermittency	56
6.2. Two-point spanwise correlation	56
Chapter 7. Summary and conclusions	64
Appendix A. Objective method for calculating boundary layer parameters	66
Acknowledgements	75
References	76

CHAPTER 1

Introduction

Investigating a solid body which is subjected to a fluid flow has been interesting for both engineers and scientists for a long time. In all cases, a thin low-speed region is formed around the body which is called *boundary layer*. Many interesting phenomena can take place inside a boundary layer. Skin friction, heat transfer and mass transfer are phenomena, which totally depend on the boundary layer behavior. By considering the uncountable cases where a solid body and fluid move in contact with each other (cars, airplanes, turbines, pipes etc.) one can realize the importance of boundary layer investigations. The simplest case is where a fluid flow passes over a flat plate with no pressure gradient. Although this case is not practically useful, it is a really proper starting point for fundamental investigations. In this case three different regimes can be recognized; laminar, transitional and turbulent region. At the beginning the boundary layer is completely predictable and the velocity fluctuations are negligible. In this region which is called laminar boundary layer, the velocity profile, skin friction and many other quantities follow the Blasius equation, when considering a zero pressure gradient flow. On the other hand, in most of the real cases, it is impossible to avoid noise which always exists and may trigger disturbances. These disturbances can enter into the laminar boundary layer and may grow in amplitude causing modulations in the base flow. It is in the transition region where this process happens. The source of disturbances can vary, common sources are surface roughness and high velocity fluctuation levels in a broad frequency spectrum, in the free-stream, which is called free-stream turbulence (FST). Taylor (1939) was one of the first ones reporting some experimental FST transitional boundary layer results. Arnal & Juillen (1978) depicted that at high free-stream turbulence intensity (above 1%), the disturbances caused by FST play a major role in the transition process rather than the TS-wave disturbances. The "*bypass transition*" expression has been used to denote this kind of transition (Morkovin 1969). Furthermore, Arnal & Juillen cited that maximum u_{rms} occurs almost at the middle of the boundary layer. Kendall (1985) was the one showing some spanwise scales along streamwise direction and called them Klebonoff modes after the pioneering work by Klebanoff (1971). Now, the free-stream turbulence is known to induce unsteady streamwise streaks of alternating low and high speed through

the lift-up mechanism (Landahl 1980) inside a laminar boundary layer. In addition, Kendall mentioned that the maximum u_{rms} inside the boundary layer grows as $x^{1/2}$. This sort of increase, so-called algebraic growth was confirmed theoretically by Andersson, Berggren & Henningson (1999) by considering the disturbance growth from an initial perturbation calculated using the optimal perturbation theory. A thorough experimental work on the FST induced transition in boundary layer was performed by Westin (1997). Westin, Boiko, B. G. B. Klingmann & Alfredsson (1994) reported that u_{rms} has a linear increase with the Reynolds number $R (= 1.72 \cdot (xU_\infty/\nu)^{1/2})$. Furthermore, it was emphasized that the growth in the streamwise direction has different rates depending on the case. In Westin, Bakchinov, Kozlov & Alfredsson (1998) the turbulence receptivity process is explained where the streaks breakdown and turbulent spot is formed. Instead of u_{rms} , one can consider energy (u_{rms}^2) as an alternative quantity. Therefore, the energy inside the boundary layer grows linearly with the downstream distance from the leading edge and when the disturbance level is high enough it will be susceptible to secondary instabilities, which locally will give birth to turbulent spots and the breakdown to turbulence is initiated. Although Matsubara & Alfredsson (2001) showed that the spanwise scales of streaks decrease by increasing the turbulence intensity (Tu) at the free-stream, Fransson & Alfredsson (2003) mentioned that in an asymptotic suction boundary layer, by changing the boundary layer thickness with a factor of two, the spanwise scales of the streaks remained constant.

There exists a numerous amount of empirical relationships between the location of transition onset and the Tu in a flat plate boundary layer, but more recent investigations have shown that the Tu -level is not the only dependent variable. An increase in the FST integral length scale Λ_x has shown, both in experiments and numerical simulations (Jonas *et al.* 2000; Brandt *et al.* 2004; Ovchinnikov *et al.* 2004) to advance the transition location. However, so far too little data has been available to draw any conclusions on how the transitional Reynolds number correlates with Λ_x .

Fransson *et al.* (2005) performed a set of experiments and reported some data about the location and length of transition caused by FST. In the present investigation, new grids were designed and manufactured to produce different free-stream turbulence characteristic (Chapter 3). Then, with a fast detection, the location of maximum disturbances from the wall was obtained and spanwise measurements carried out in few distances from the leading edge to find out the spanwise wavelengths of the streaky structures (Chapter 6). The next step, streamwise measurements were done and the data were evaluated to find the onset and length of transition region. These values were connected to the FST characteristics at the leading edge and were scaled in a way to have a universal pattern. Other quantities such as energy and higher velocity moments are also evaluated (Chapter 4). In addition, wall-normal measurements were done

in order to sweep the transitional boundary layer in three dimensions and intermittency and higher order velocity moments were calculated (Chapter 5).

Experimental facility and measurement technique

2.1. The wind tunnel facility

All the experiments were performed in the Minimum Turbulence Level (MTL) wind tunnel located at the Royal Institute of Technology (KTH) in Stockholm. MTL is a closed circuit wind tunnel with a 7 metre long test section and $0.8 \times 1.2 \text{ m}^2$ (height \times width) cross-sectional area. An axial fan (DC 85 kW) can produce airflow in the empty test section with a speed up to 70 m/s. To keep the airflow temperature constant ($20 \text{ }^\circ\text{C}$), a cooling system was employed with the accuracy of ($\pm 0.1 \text{ }^\circ\text{C}$) at a 6 m/s free-stream velocity, which was the velocity in the present investigation. A sketch of the wind tunnel is shown in figure 2.1.

The experiments were carried out over a 5 metre-long flat plate. To minimize the leading edge effect, a trailing flap with a 6° angle was used along with an asymmetric leading edge with an aspect ratio of 12. The wind-tunnel ceiling contains 6 adjustable parts providing the ability of obtaining a zero pressure gradient. The best aspect of the MTL is the background turbulence intensity level. At 25 m/s, a 0.025% streamwise turbulence intensity was reported by Lindgren & Johansson (2002). The honeycomb, the screens and the contraction ratio (9 : 1) along with the specially designed guiding vanes in the corners are the reasons for this nice flow quality.

In addition, a traversing system with five degrees of freedom, makes it possible to, for instance, perform X -probe hot-wire calibration *in-situ*. The traversing directions are: the streamwise direction (X), the wall-normal (Y) and the spanwise (Z) directions. The other degrees of freedom are rotational directions around the Y -axis (or possibly the Z -axis) (α) and the X -axis (φ). The traversing system is controlled by a computer, which is mastered by the measuring computer.

2.2. Measurement technique

A hot-wire anemometry system was employed to measure the three velocity components (U , V , W) corresponding to the (X , Y , Z) directions. Heating a wire subjected to an airflow is the main principle of hot-wire anemometry. In the constant temperature anemometry (CTA) mode, the hot-wire temperature is held constant. In this case, higher speed increases convection heat-transfer

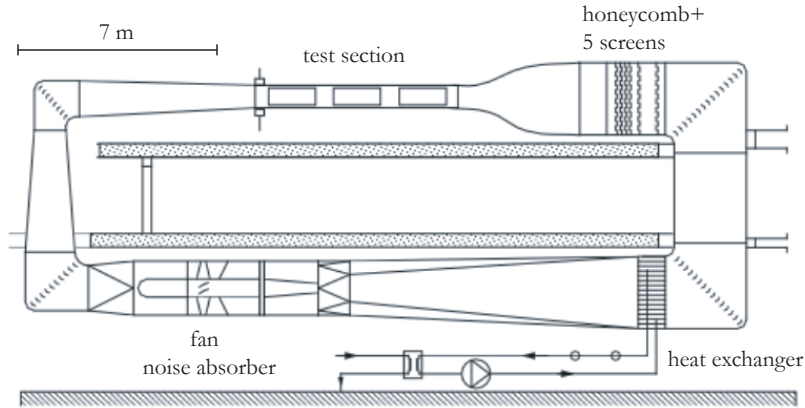


FIGURE 2.1. A sketch of the MTL wind tunnel.

and so for satisfying constant temperature, higher voltage has to be applied to the top of the bridge of the anemometry circuit. Many different calibration functions can be employed. Here, we use the modified King's law (Johansson & Alfredsson 1982), which has an extra term compensating for natural heat convection from the wire at low velocities. The law is in the form

$$U = k_1(E^2 - E_0^2)^{1/n} + k_2(E - E_0)^{1/2} , \quad (2.1)$$

where E and E_0 are the voltage at instantaneous speed and the voltage at zero speed, respectively. In addition, k_1 , k_2 and n are calibration coefficients determined in the calibration. In the calibration, the single hot-wire probe was perpendicularly subjected to an airflow and the voltage output was calibrated against the velocity measured by a Prandtl tube. A typical calibration consisted of 15 calibration points in the range 0 – 7 m/s . In figure 2.2 the output, relating voltage to velocity, from a calibration is shown. The single wire sensor was made *in-house* of a Wollaston Platinum wire of 2.54 μm in diameter and 0.7 mm long.

Furthermore, a dual-sensor probe in shape of an X was used to measure two velocity components simultaneously. This probe was employed to measure the anisotropy of the free-stream turbulence. For an X -probe calibration, the wires were subjected to the airflow with different angles between -30° and $+30^\circ$ with a 5° step. The speed range was between 5 to 7 m/s . A two-dimensional fifth-order polynomial was used as calibration function. The general form of these polynomials for the streamwise U and the spanwise W components are

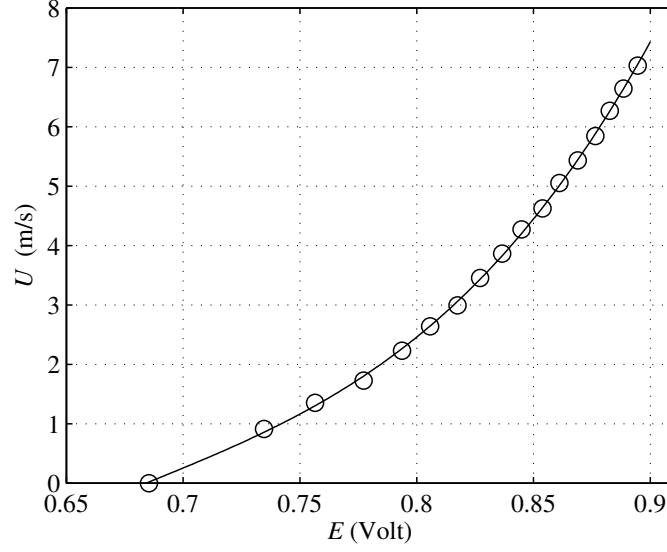


FIGURE 2.2. A typical relation voltage versus velocity for a single hot-wire probe.

$$\begin{aligned}
 U &= \sum_{i=0}^5 \sum_{j=0}^i a_{i,j} X^i Y^{i-j} \\
 W &= \sum_{i=0}^5 \sum_{j=0}^i b_{i,j} X^i Y^{i-j} ,
 \end{aligned} \tag{2.2}$$

where $X = E_1 + E_2$ and $Y = E_1 - E_2$. By fitting the data obtained from the calibration into the equations 2.2, the coefficients, $a_{i,j}$ and $b_{i,j}$, are determined. A typical graph of E_1 versus E_2 for a X -probe is shown in figure 2.3. Each wire of the X -probe was made of a Wollaston Platinum wire with a $5.08 \mu\text{m}$ in diameter and 1.4 mm long. Depending on the orientation of the X -probe it can equally measure the V velocity component instead of the W component along with the U component.

In all the experiments, a DANTEC Dynamics™ StreamLine 90N10 Frame anemometer system was employed and the signals were acquired by a National Instruments™ convertor board (NI PCI-6259, 16-Bit) with a sampling frequency of 10 kHz. Beside the hot-wire anemometer, a Prandtl tube was connected to a manometer (Furness FC0510) to measure the dynamic pressure during the calibration. Furthermore, the manometer used external probes for registering the temperature and the total pressure inside the test section.

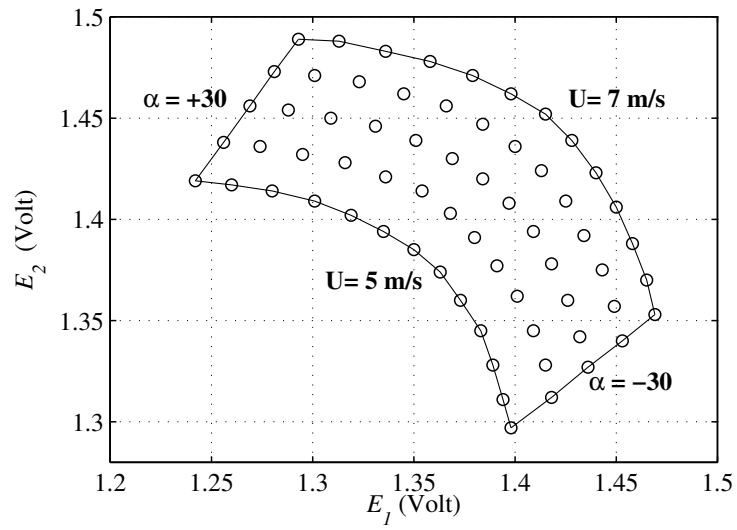


FIGURE 2.3. A typical calibration graph of E_1 versus E_2 of a dual-wire X -probe.

CHAPTER 3

Free-stream turbulence and base flow characteristics

3.1. Turbulence generating grids

The free-stream turbulence (FST) behind a turbulence generating grid may be characterized by means of its turbulence intensity (Tu), integral (Λ), Taylor (λ) and Kolmogorov (η) length scales. Free-stream turbulence intensity is defined as the ratio between the second order velocity moment and the mean free-stream velocity,

$$Tu = \frac{u_{rms}}{U_\infty} . \quad (3.1)$$

The integral length scale is the most energetic length scale, the Taylor length scale is the smallest energetic length scale and the Kolmogorov length scale is the smallest viscous scale in a turbulent flow. In order to calculate these length scales, the auto-correlation (f) and cross-correlation (g) functions are first calculated from the velocity signals and then calculated as,

$$\begin{aligned} \Lambda_x &= \int_0^\infty f \, dx , \\ \Lambda_z &= \int_0^\infty g \, dz , \\ \frac{1}{\lambda_x^2} &= -\frac{1}{2} \left[\frac{\partial^2 f}{\partial r^2} \right]_{r=0} , \\ \eta &= \left(\frac{\nu^3}{\epsilon} \right)^{1/4} . \end{aligned} \quad (3.2)$$

In this thesis the same techniques as described in Kurian & Fransson (2009) to assess above length scales were used.

One of the most important characteristics of a grid geometry is its porosity (β), which is defined as the ratio between open and total area of the grid,

$$\beta = \left(1 - \frac{d}{M} \right)^2 , \quad (3.3)$$

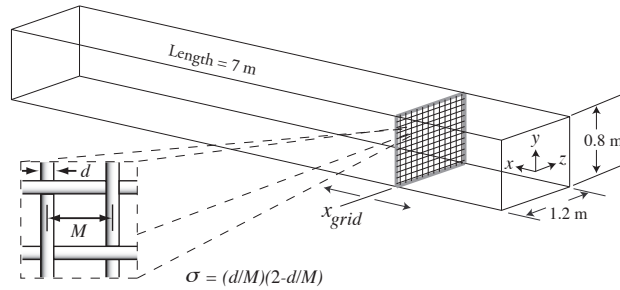


FIGURE 3.1. A sketch of a typical grid inside the wind tunnel test section. Sketch taken from Kurian & Fransson (2009) .

where d and M are the bar diameter and the mesh width, respectively (cf. figure 3.1). The counterpart to porosity, solidity (σ), is commonly used, which is defined as $1 - \beta$.

By mounting different grids in front of the leading edge of a flat plate, different FST characteristics may be obtained. In order to get a wide range of FST characteristics, six new grids were designed and manufactured for the present investigation. Totally eight different grids were used and all of them are summarized in table 1. Figure 3.2 shows a grid which is located inside the wind tunnel before the leading edge during the experiment.

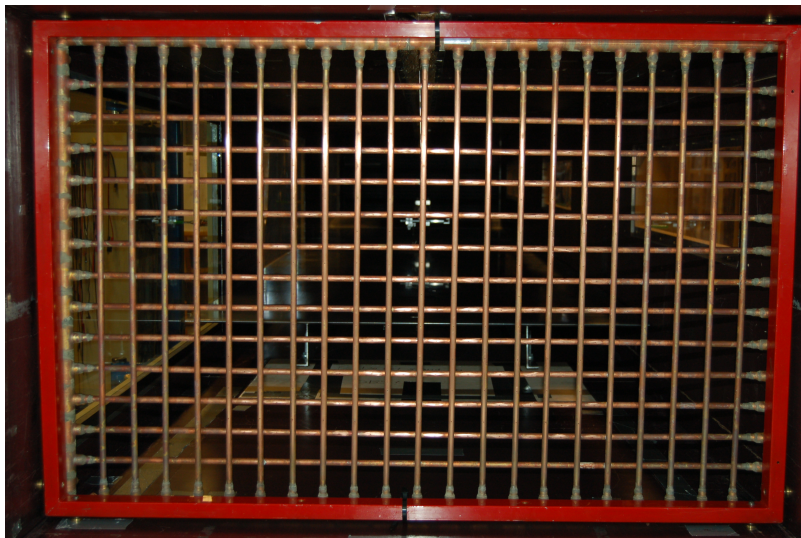


FIGURE 3.2. Grid number 2 inside the wind tunnel

	$d(\text{mm})$	$M(\text{mm})$	σ	Bar geometry	Type	C_g	Symbol
$G1$	8	40	0.360	<i>Circle</i>	<i>Active</i>	0.0254	◦
$G2$	10	50	0.360	<i>Circle</i>	<i>Active</i>	0.0304	◻
$G3$	12	60	0.360	<i>Circle</i>	<i>Active</i>	0.0063	◊
$G4$	12	50	0.422	<i>Circle</i>	<i>Active</i>	0.0096	△
$G5$	8	50	0.294	<i>Circle</i>	<i>Active</i>	0.0097	▽
$G6$	12	70	0.313	<i>Circle</i>	<i>Active</i>	0.0116	◁
$G7$	6	36	0.305	<i>Circle</i>	<i>Passive</i>	-	▷
$G8$	10	50	0.360	<i>Square</i>	<i>Passive</i>	-	★

TABLE 1. Geometrical data of all grids. d , M , σ and C_g are the bar diameter, the mesh width, the solidity and the injection coefficient, respectively.

The experiments show that the pressure drop over a grid is a function of the grid solidity. At the same time, a higher pressure drop leads to a higher turbulence intensity. This is in agreement with Gad-El-Hak & Corrsin (1974). Another way to increase the pressure drop and in turn the Tu is to inject a secondary counter-flow, relative to the free-stream, by means of upstream pointing air jets from the grid. This idea was first tested by Gad-El-Hak & Corrsin (1974) and has since then been applied successfully on other experiments (Fransson & Alfredsson 2003; Yoshioka *et al.* 2004; Fransson *et al.* 2005). The counter-flow injection is accomplished by pressurizing the new grids, which have been manufactured using copper tubes as grid bars. This type of grid we here call *active* in contrary to *passive* when the grid may not be pressurized. The six new grids are active and were designed with the motive to systematically vary the FST characteristics. Note here that the new grids are G1–6 while grids G7 and G8 are two passive grids, which have been used in previous FST experiments in the MTL wind tunnel. Three of the grids have the same solidity but different bar diameters and mesh widths (G1–3) and three have the same mesh width but different bar diameters and hence different solidities (G2, 4 and 5). Grid 6 is designed for low Tu but large length scales, relative to G1–4. Note that G5 has almost the same solidity as G6 but with the aim to generate smaller scales.

The secondary air flow was obtained from a fan and carried by eight hoses to the grids. A regulating valve was employed to adjust the pressure inside the grids leading to controlled injection speeds. The grids have different numbers of orifices, i.e. upstream pointing jets, but with the same diameter of 1.5 mm. The pressures and the injection rates were measured by a differential manometer and a flowmeter respectively. Figure 3.3 demonstrates how the injection speed varies with the relative pressure inside the grids (P_g). Equation 3.4 shows the relation between them for different grids with the same orifice diameter,

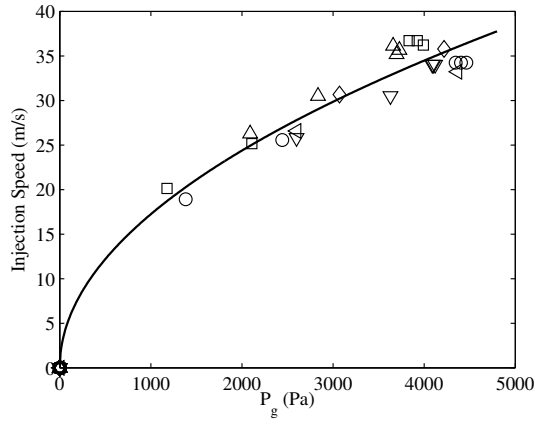


FIGURE 3.3. Injection speed vs grid pressure. The solid line corresponds equation 3.4.

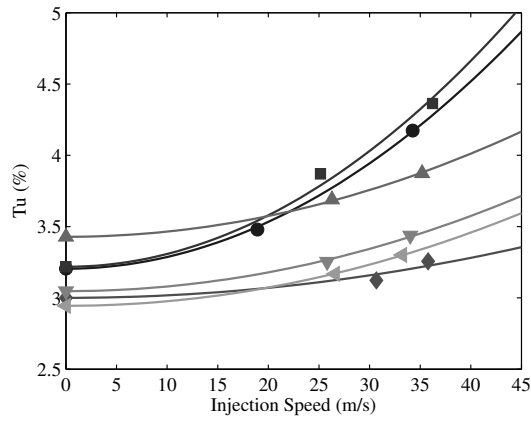


FIGURE 3.4. The turbulence intensity versus the injection speed.

$$U_{inj} = 0.54 \sqrt{P_g}, \tag{3.4}$$

where the coefficient 0.54 has been determined in a least square fit sense to the data in figure 3.3.

Furthermore, the injection speed is correlated to the turbulence intensity. But the effect of injection is different among the grids. It is likely that all the grids follow the relation,

$$Tu = Tu_0 + C_g \left(\frac{U_{inj}}{U_\infty} \right)^2, \quad (3.5)$$

where Tu_0 is the turbulence intensity without any injection and different C_g values which are given in table 1 and determined in a least square fit sense to the data. In addition, by locating the grids at different distances from the leading edge, different turbulence intensities and integral length scales were obtained. Setting a grid close to the leading edge higher turbulence intensities would be available, but there is a rule of thumb of about 20-mesh-widths, which is required in order to obtain a close to homogeneous turbulence. Note, that for most grids a downstream distance of over 60 mesh-widths is required in order to reach a "fully" developed FST implying saturated anisotropy measures (Kurian & Fransson 2009).

3.2. Free-stream turbulence characteristics

As previously mentioned, eight turbulence generating grids were used, six of which were active and two passive. By applying different injection rates of the active grids and by varying the upstream location of the grids relative to the leading edge, 42 cases were obtained, all which are presented in table 2. All the grids, except for G3 and G7, were positioned at three different locations. The closest distance corresponded to $X_{grid}/M = 20$, where X_{grid} corresponds to the distance between the grid and the leading edge. The maximum distance was 1400 mm upstream of the leading edge, which was limited by the beginning of the contraction. Note that the 20-mesh-widths of the G3 is close to 1400 mm, so only one upstream location of that grid was investigated, i.e. $X_{grid} = 1300$ mm corresponding to $X_{grid}/M = 21.5$. The passive grid G7 has a special design, which only allows the grid to be positioned in one location $X_{grid} = 1710$ mm correspond to $X_{grid}/M = 47.5$. For all active grids, beside the zero injection case, two other cases with different injection rates were investigated: the maximum possible injection rate (*Max*) and an intermediate injection (*Mid*). The turbulence intensity (Tu), the longitudinal integral length scale (Λ_x), the Taylor length scale (λ_x), the transverse integral length scale (Λ_z) and the anisotropy were measured at the leading edge in the free-stream as a reference, and are summarized in table 2. All the measurements were done with two hot-wires separated with a certain distance, which allows continuous comparison between the two. The results from the two probes in table 2 are indicated with an index 1 and 2.

For simplicity, many theoretical turbulence relations have assumed isotropic and homogeneous turbulence. The FST generated behind a grid is usually anisotropic and inhomogeneous, so it becomes important to characterize this. By using an X hot-wire probe anisotropy measurements could be carried out. Figures 3.5 and 3.6 show the results of the two anisotropy measures v_{rms}/u_{rms} and w_{rms}/u_{rms} , respectively, for all cases. Although for the cases with high

solidity the anisotropy measures are around unity, i.e. close to isotropic turbulence, low solidity grids have typically low anisotropy measures (as low as 0.8) and hence are fairly anisotropic.

In addition, for one of the cases (G1 and $X_{grid} = 800$ mm and maximum injection) the homogeneity was measured in the free-stream at the leading edge. For this purpose the X hot-wire probes was traversed in the yz -plane. The contour lines of the anisotropy measures show the homogeneity in the cross sectional plane and are illustrated in figures 3.7 and 3.8.

<i>Grid</i>	X_{Grid} (cm)	<i>Injection</i>	Tu_1 (%)	Tu_2 (%)	Λ_{x1} (mm)	Λ_{x2} (mm)	Λ_z (mm)	λ_{x1} (mm)	λ_{x2} (mm)	$\frac{u_{rms}}{u_{rms}}$	$\frac{w_{rms}}{u_{rms}}$
G1	80	0	3.1169	3.2923	17.7885	17.4172	8.5754	11.9301	11.8719	0.8139	0.8859
G1	80	<i>Mid</i>	3.4652	3.4934	16.5810	16.0540	9.1670	12.2690	11.7771	0.8129	0.8614
G1	80	<i>Max</i>	4.2189	4.1280	20.1914	19.2089	10.1727	13.1813	12.4591	0.7942	0.8611
G1	110	0	2.4247	2.6169	18.2726	18.3894	9.6300	12.3088	12.5638	0.8162	0.8878
G1	110	<i>Max</i>	3.2965	3.3167	20.3580	20.0298	10.8150	13.0368	12.8751	0.8028	0.8637
G1	140	0	2.0843	2.1820	19.5955	19.5521	11.0770	12.9707	12.9284	0.8271	0.9132
G1	140	<i>Mid</i>	2.4510	2.5057	19.7231	20.2219	11.0855	12.9732	12.9989	0.8234	0.8805
G1	140	<i>Max</i>	2.8225	2.8673	21.9463	21.9129	12.1831	13.5179	13.3843	0.8130	0.8617
G2	100	0	3.1269	3.3088	19.0354	19.4371	9.6402	12.2934	12.3867	0.9150	0.8841
G2	100	<i>Mid</i>	3.7924	3.9458	20.2611	19.6972	10.0459	13.0502	12.8360	0.8776	0.9235
G2	100	<i>Max</i>	4.3188	4.4070	22.6171	21.7028	11.3043	13.7094	13.3342	0.8551	0.9010
G2	120	0	2.6827	2.8208	21.2025	20.8190	10.3859	12.8401	12.6946	0.9195	0.9018
G2	120	<i>Max</i>	3.8116	4.0400	23.3907	23.0796	12.1378	13.9841	13.8648	0.8642	0.8955
G2	140	0	2.4391	2.5559	21.2396	21.2124	10.6538	13.1248	12.9777	0.9228	0.8967
G2	140	<i>Mid</i>	2.8402	2.9589	21.7296	20.9263	11.1854	13.8197	13.5033	0.9147	0.9205
G2	140	<i>Max</i>	3.4364	3.6294	24.6696	24.4583	13.3687	14.4665	14.3678	0.8731	0.9308
G3	130	0	2.9400	3.0604	22.7070	21.8221	11.9267	13.2710	13.1189	0.9228	0.9530
G3	130	<i>Mid</i>	3.0717	3.1733	21.8418	21.0620	11.6116	13.3103	12.9823	0.9304	0.9289
G3	130	<i>Max</i>	3.2060	3.3065	22.7884	22.0271	12.0283	13.4818	13.1568	0.9165	0.9397
G4	100	0	3.3091	3.5478	20.0229	19.6744	10.9966	12.7887	12.8919	0.8941	0.9539
G4	100	<i>Mid</i>	3.6025	3.7773	21.4318	20.0140	10.5524	13.0363	12.8181	0.9244	0.9641
G4	100	<i>Max</i>	3.7836	3.9636	22.1424	20.9476	11.2483	13.1572	13.0344	0.9269	0.9569
G4	120	0	3.0321	3.3483	21.0015	20.4546	10.9678	12.9991	12.9821	0.9098	0.9645
G4	120	<i>Max</i>	3.3394	3.6471	21.8066	20.9749	10.3994	13.0873	13.0612	0.9538	0.9680
G4	140	0	2.7631	2.9910	22.6133	22.0751	12.7500	13.8024	13.7105	0.9197	0.9626
G4	140	<i>Mid</i>	2.8930	3.0880	23.3316	22.2555	12.7078	13.8164	13.5278	0.9465	0.9645
G4	140	<i>Max</i>	3.0561	3.2048	24.1457	22.5083	12.1289	13.9984	13.6001	0.9540	0.9574

<i>Grid</i>	X_{Grid} (cm)	<i>Injection</i>	Tu_1 (%)	Tu_2 (%)	Λ_{x1} (mm)	Λ_{x2} (mm)	Λ_z (mm)	λ_{x1} (mm)	λ_{x2} (mm)	$\frac{u_{rms}}{u_{rms}}$	$\frac{w_{rms}}{u_{rms}}$
G5	100	0	2.8738	3.2203	18.4947	19.4507	7.3708	11.8882	11.9493	0.8698	0.8770
G5	100	<i>Mid</i>	3.1681	3.3388	16.2912	16.2879	7.5709	11.8271	11.7297	0.8878	0.8545
G5	100	<i>Max</i>	3.3324	3.5418	17.6857	17.7534	8.9516	12.2381	12.0887	0.8749	0.8638
G5	120	0	2.3624	2.6319	20.7000	19.9904	8.8047	12.3591	12.3150	0.8806	0.8779
G5	120	<i>Max</i>	2.7896	3.0010	19.2964	18.9484	9.8748	12.6229	12.4848	0.8768	0.8697
G5	140	0	2.1670	2.4642	22.0074	22.7535	10.7700	12.8739	12.9280	0.8922	0.8938
G5	140	<i>Mid</i>	2.4174	2.5879	19.9966	19.6279	10.3880	12.8926	12.6794	0.9062	0.8803
G5	140	<i>Max</i>	2.4736	2.6467	20.6013	20.0980	10.8651	13.0561	12.7753	0.8994	0.8802
G6	140	0	2.8328	3.0556	22.2742	22.8199	10.7273	13.1285	13.0533	0.9105	0.9142
G6	140	<i>Mid</i>	3.0515	3.2852	20.8117	20.5363	10.1025	12.9973	12.9112	0.8864	0.8633
G6	140	<i>Max</i>	3.1981	3.4044	21.8996	21.4789	10.6405	13.2510	13.0283	0.9018	0.8775
G7	171	0	1.8151	1.7808	18.4638	18.8618	8.5675	12.9596	12.3948	0.8629	0.8256
G8	100	0	5.6406	5.9181	24.2281	22.8491	11.8935	13.9659	13.6359	0.8547	0.8238
G8	120	0	5.1396	5.3028	25.3589	23.8901	12.4693	14.2315	13.9024	0.8627	0.8451
G8	140	0	4.5360	4.6683	25.6081	24.3217	12.5562	14.3095	13.9900	0.8643	0.8477

TABLE 2. Free stream characteristic at the leading edge. Index 1 and 2 represent hot-wire 1 and 2.

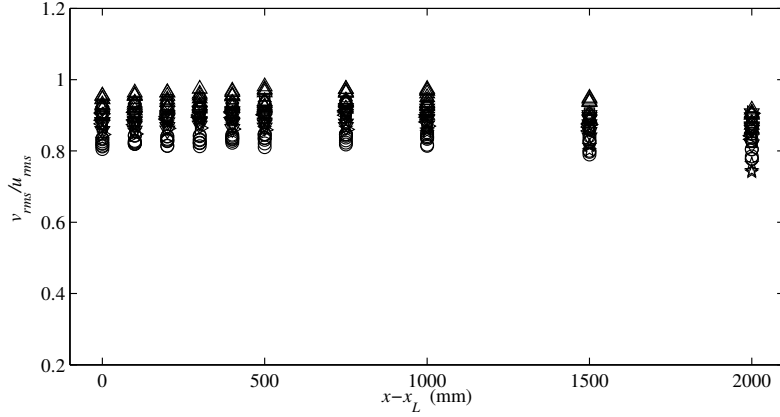


FIGURE 3.5. Wall-normal component anisotropy measure for all the cases in the streamwise direction.

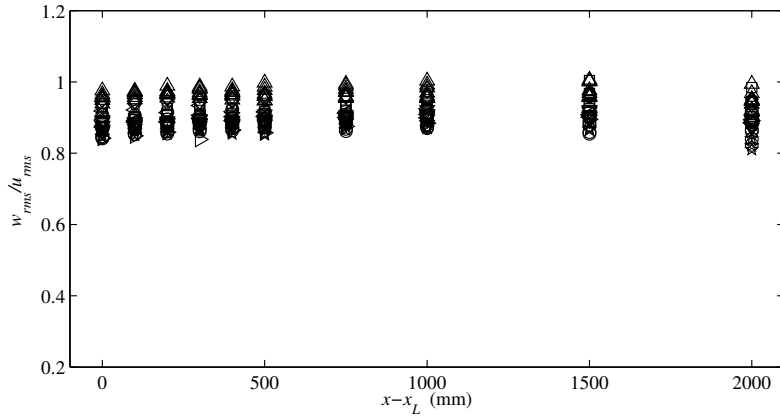


FIGURE 3.6. Spanwise component anisotropy measure for all the cases in the streamwise direction.

In figure 3.9, the evolution of the turbulence intensity in streamwise direction is shown for all 42 cases. One may observe that, the intensities decrease along x with a typical power law decay according to (Batchelor & Townsend 1948),

$$Tu = \mathcal{A} \left(\frac{x - x_0}{M} \right)^m. \quad (3.6)$$

In this equation, x_0 is a virtual origin which is defined as the location where the intensity asymptotes to infinity and \mathcal{A} describes the level of Tu .

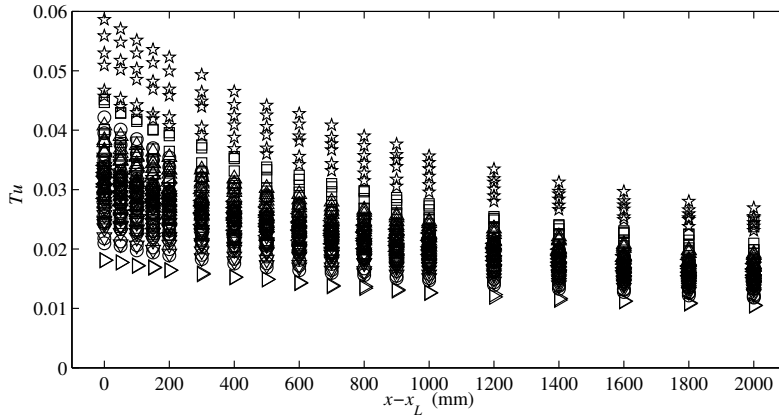


FIGURE 3.9. Turbulence intensity decay in the streamwise direction. x_L corresponds to the distance between the grid and the leading edge in each case.

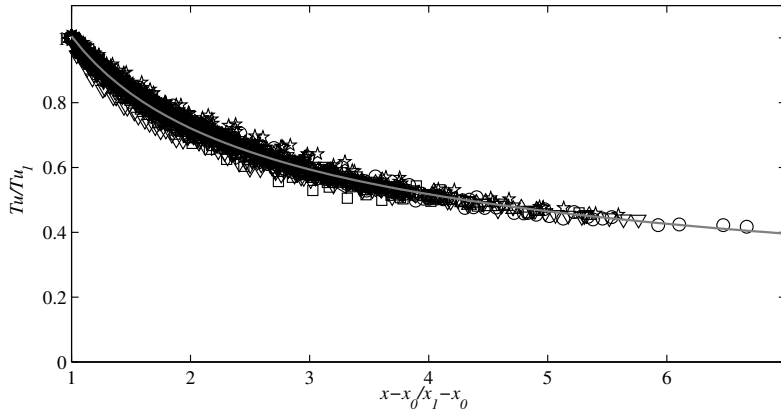


FIGURE 3.10. Normalized intensity decay in the streamwise direction. x_0 is the virtual origin and Tu_1 is the intensity at x_1 . The solid line correspond to equation 3.7 with $m_{Tu} = -0.48$.

location x_1 . In figure 3.9, x_1 was chosen as the minimum distance from the grid.

$$\frac{Tu}{Tu_1} = \left(\frac{x - x_0}{x_1 - x_0} \right)^{m_{Tu}} \tag{3.7}$$

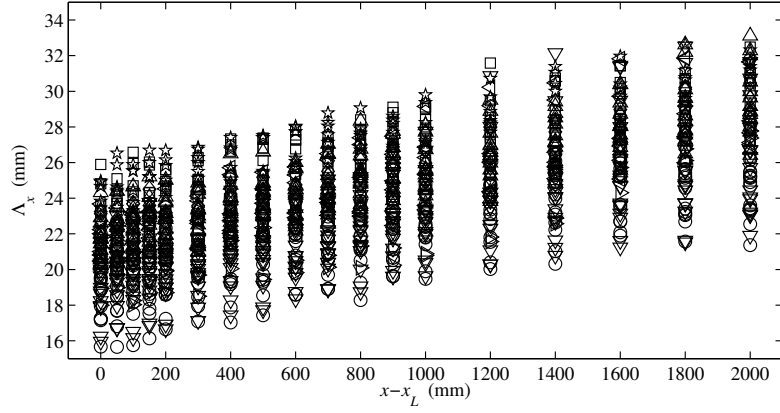


FIGURE 3.11. Longitudinal integral length scale growth in streamwise direction. x_L represents the leading edge location.

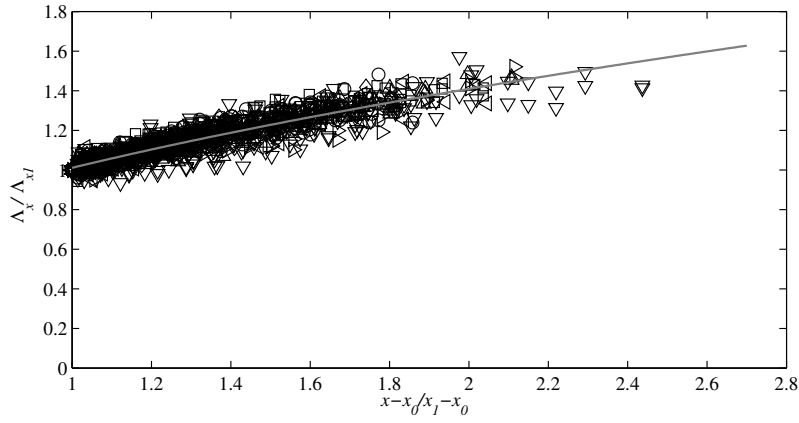


FIGURE 3.12. Normalized longitudinal integral length scale distribution in the streamwise direction. x_0 is the virtual origin and Λ_{x_1} is the longitudinal integral length scale at $x = x_1$. The solid line correspond to equation 3.8 with $m_\Lambda=0.48$.

The exponent is determined to $m_{T_u} = -0.48$ when the equation 3.7 is fitted in a least square sense to the experimental data. Figure 3.10 provides all the normalized intensity decays in the form 3.7.

In figure 3.11 the streamwise evaluation of the longitudinal integral length scale is shown for all the 42 cases. The same normalization as was done for the turbulence intensity, with a virtual origin (x_0) defined where Λ_x is equal to zero. Considering all cases the virtual origin vary between -2500 mm to

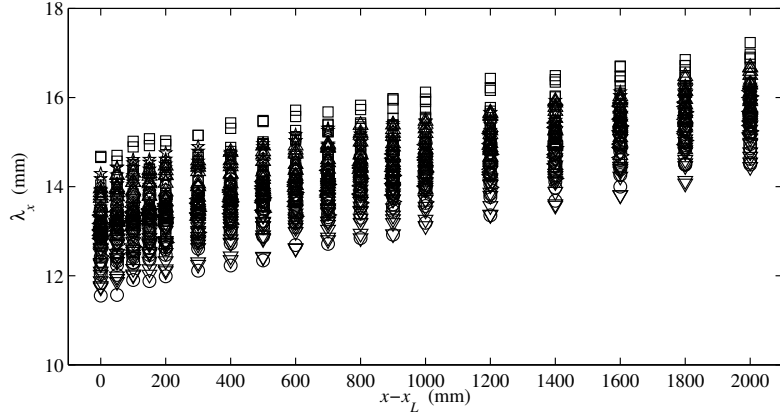


FIGURE 3.13. Longitudinal Taylor length scale distribution in the streamwise direction. x_L represents the leading edge location.

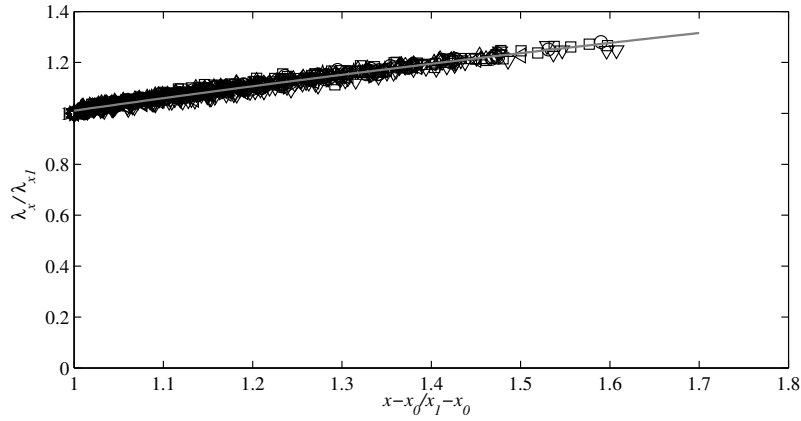


FIGURE 3.14. Longitudinal Taylor length scale growth in the streamwise direction.

190 mm from the grid location. Furthermore, Λ_{x_1} is the longitudinal integral length scale at $x = x_1$. Here, x_1 was chosen as the minimum distance from the grid. In figure 3.12 the normalized data, according to,

$$\frac{\Lambda_x}{\Lambda_{x_1}} = \left(\frac{x - x_0}{x_1 - x_0} \right)^{m_\Lambda}, \quad (3.8)$$

is shown. Determining the exponent m_Λ in a least square fit sense to the data gives $m_\Lambda = 0.48$, i.e. $m_\Lambda = -m_{Tu}$.

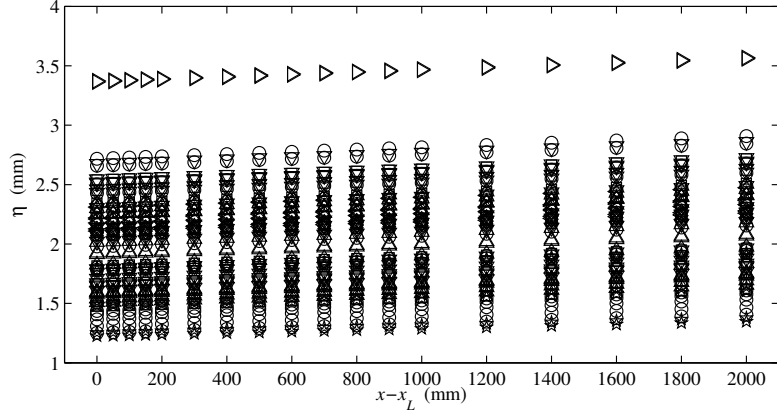


FIGURE 3.15. Kolmogorov length scale distribution in the streamwise direction. x_L represents the leading edge location.

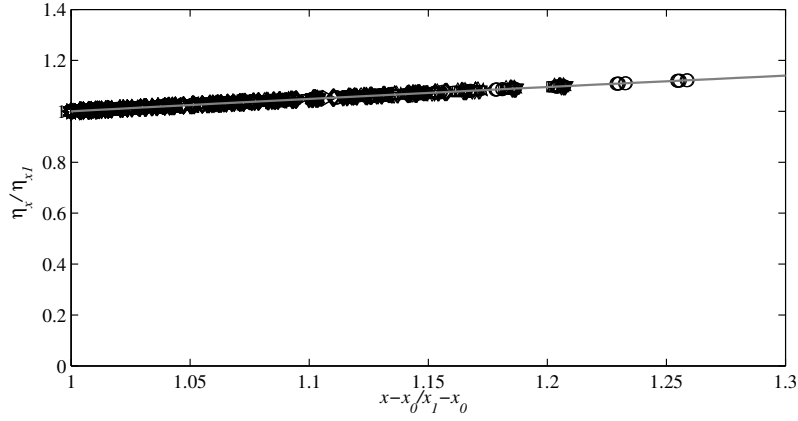


FIGURE 3.16. Kolmogorov length scale growth in the streamwise direction.

Although the curve fit shows the trend of a power law growth, there is some scatter, specially far downstream.

Again, the same normalization is applied on the Taylor length scale data. In figure 3.13 and 3.14 the absolute data and the normalized data are plotted, respectively. The exponent m_λ in relation 3.9 becomes 0.50 when fitted to the data.

$$\frac{\lambda_x}{\lambda_{x1}} = \left(\frac{x - x_0}{x_1 - x_0} \right)^{m_\lambda}. \quad (3.9)$$

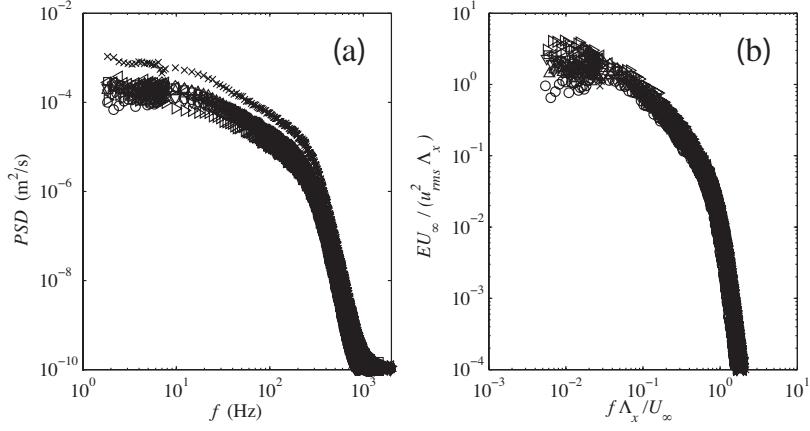


FIGURE 3.17. (a) shows the power spectra for all grids without injection at the leading edge. (b) Non-dimensional form of the data in (a).

The smallest length scale (Kolmogorov length scale) can be estimated simply by calculating the dissipation rate as,

$$\epsilon = -\frac{3}{2}U_\infty \frac{du_{rms}^2}{dx} \quad (3.10)$$

and using the last equation in (3.2). Figures 3.15 and 3.16 show the evolution of Kolmogorov length scale in the absolute form and normalized values, respectively. The exponent of $m_\eta = 0.5$ in equation 3.11 gives the best data fitting and is shown in figure 3.16,

$$\frac{\eta_x}{\eta_{x1}} = \left(\frac{x - x_0}{x_1 - x_0} \right)^{m_\eta}. \quad (3.11)$$

The power spectral density (PSD) can be calculated from a signal and shows how the power is distributed based on frequency. A typical PSD diagram is shown in figure 3.17 and it is seen that in the region of $f \gtrsim 500$ Hz the power is really low and hence negligible. In figure 3.17 (a) the dimensional power spectra in the free-stream are shown for each grid without injection and at the leading edge. The non-dimensional spectra are shown in figure 3.17 (b).

A better view of the energy distribution is presented in figure 3.18, which shows the corresponding pre-multiplied spectra shown in the figure 3.17. In figure 3.18 the percentage of the total energy in each frequency is given. The maximum energy for these cases are distributed in the range $10 < f < 100$ Hz.

In order to elucidate the effect of injection on the energy content at different frequencies, the pre-multiplied power spectra are compared for one grid (G5) at

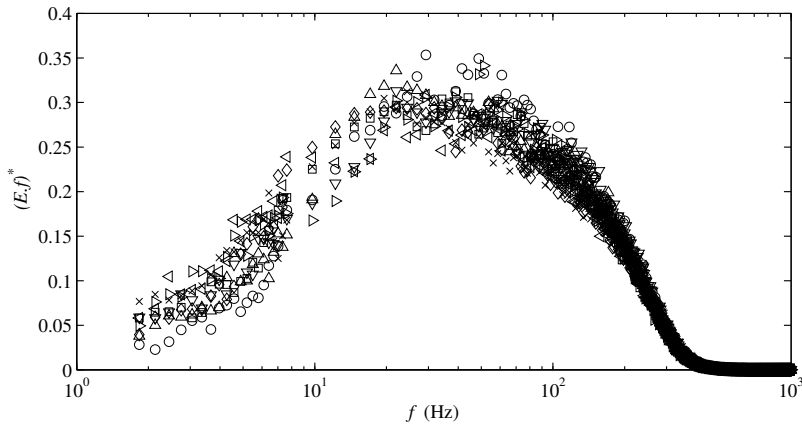


FIGURE 3.18. Typical pre-multiplied energy distribution at the leading edge for all grids.

different downstream locations of the grid. The dotted, dashed and solid lines correspond to the natural case (without injection), MID injection and MAX injection, respectively. The vertical lines indicate the frequency of maximum energy at $x = 1000$ mm for each case. These vertical lines are then kept as references for $x = 1500$, 2000 and 3000 mm in order to reveal changes in the energy distributions. Firstly one may observe that the injection has little effect on the energy distribution when the injection is increased. Secondly, the spectra move slightly towards larger scales with downstream distances, which is in line with an increase of the integral length scale with x .

Figures 3.20, 3.21 and 3.22 show the leading edge turbulence characteristics, for the different grids, in terms of their turbulence intensity, integral length scale and the Taylor length scale, respectively, when located at $X_{grid}/M \approx 20$. Note that the new grids G1–6 produce almost the same turbulence intensity (cf. figure 3.20) in the default scenario, but different integral length and Taylor length scales, cf. figures 3.21 and 3.22, respectively. In these figures, the G7 is not considered. The reason is that it is impossible to locate G7 at $X_{grid}/M \approx 20$.

3.3. Base flow characteristics

When experimentally studying boundary layer stability and transition to turbulence, it is important to reduce the number of influencing parameters. It is well known that with an asymmetric leading edge of the flat plate one may get rid of the adverse pressure gradient region and minimize the favorable pressure gradient region in the streamwise direction, which arise on any symmetric body (Klingmann *et al.* 1993; Fransson 2004). The ideal developing boundary layer for stability and transition experiments is the one developing under zero pressure gradient, the so called Blasius boundary layer. A numerical solution

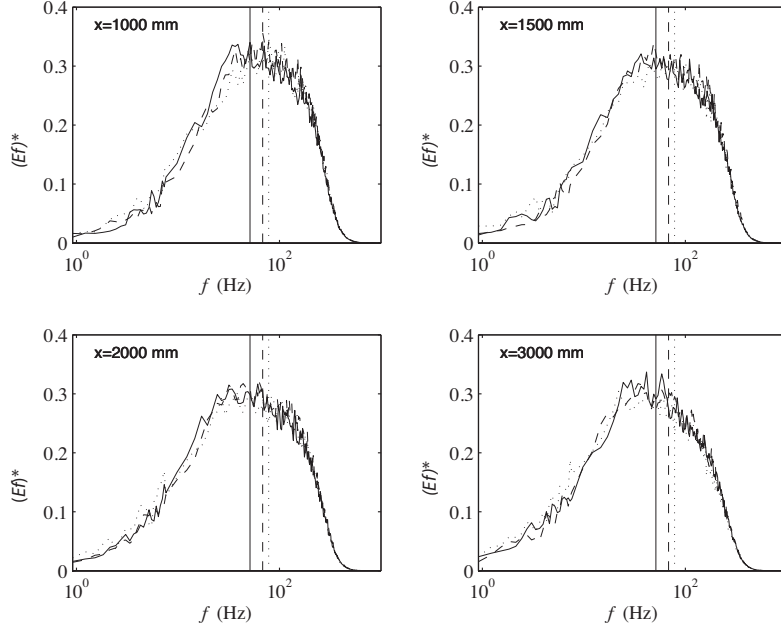


FIGURE 3.19. Pre-multiplied energy spectra for G5 at different downstream locations. $x = 1000$ mm correspond to the leading edge of the flat plate. Dotted, dashed and solid lines correspond to no injection, Mid and Max injection, respectively. Vertical lines indicate their corresponding energy maxima.

to this boundary layer may be obtained by solving the Blasius equation, which is readily derived from the boundary layer equation by introducing a stream-function (ψ) and using the concept of similarity,

$$\psi(x, y) = f(\eta)\sqrt{\nu U_\infty x}, \quad (3.12)$$

where $f(\eta)$ is the similarity function with $\eta (= y/\delta)$ being the dimensionless wall-normal coordinate. Here, $\delta = \sqrt{x\nu/U_\infty}$ is the boundary layer length scale. The Blasius equation becomes,

$$f''' + \frac{1}{2}ff'' = 0, \quad (3.13)$$

with the boundary conditions $f(0) = 0$, $f'(0) = 0$ and $f(\infty) = 1$. The two first correspond to the impermeable and the no-slip conditions at the wall, respectively, and the latter to the free-stream condition.

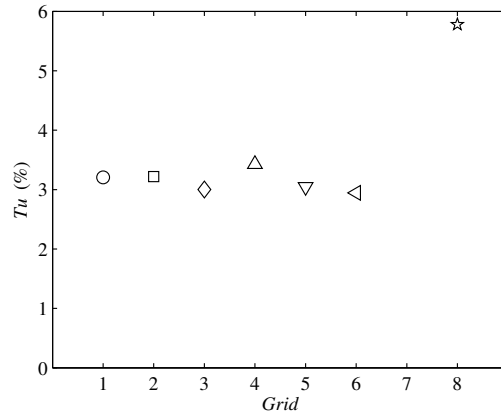


FIGURE 3.20. Turbulence intensities at the leading edge when $x/M \approx 20$ and without injection.

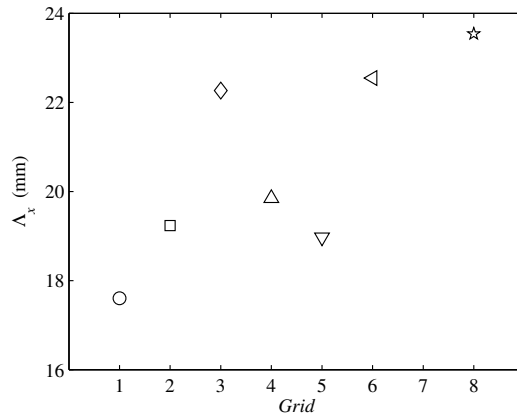


FIGURE 3.21. Integral length scales at the leading edge when $x/M \approx 20$ and without injection.

For comparison with other experiments, it is important to characterize the base flow, i.e to quantify how Blasius-like the investigated boundary layer is. The best measures for this are the boundary layer parameters such as the displacement (δ_1) and momentum (δ_2) thicknesses, which are integral length scales and defined as

$$\delta_1 = \int_0^{\infty} \left(1 - \frac{U(y)}{U_{\infty}}\right) dy$$

and

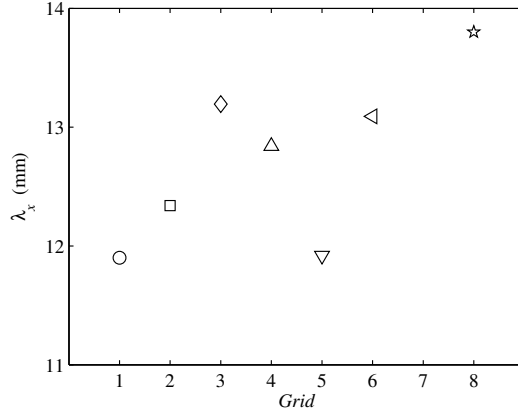


FIGURE 3.22. Taylor length scales at the leading edge when $x/M \approx 20$ and without injection.

$$\delta_2 = \int_0^\infty \frac{U(y)}{U_\infty} \left(1 - \frac{U(y)}{U_\infty} \right) dy, \quad (3.14)$$

respectively, along with their ratio $H = \delta_1/\delta_2$, which is the shape factor of the mean velocity profile.

For reasons mentioned above the pressure gradient was set with the aim of having a zero pressure gradient, by adjusting the ceiling of the test-section along with the trailing edge flap of the plate. Figure 3.23 shows the pressure coefficient ($C_p = 1 - (U/U_\infty)^2$) variation in the streamwise direction from the leading edge. After the leading edge effect ($x > 200$ mm) a variation of about 1% in C_p is observed along x .

The effect of a favorable pressure gradient ($dP/dx < 0$) on the stability and the transition is stabilizing meaning that the transition onset will be delayed. The adverse pressure gradient ($dP/dx > 0$) will have the opposite effect.

The quality of the experimental setup may be validated by looking at the experimentally measured mean velocity profiles in the wall-normal direction and compared to the numerical solution to equation 3.13. In figure 3.24 seven profiles taken at different streamwise locations along the plate are shown with the solid line corresponding to the Blasius solution. An even more qualitative validation would be to compare the integral length scales and their ratio, which is done in figure 3.25. Note that the solid lines correspond to the theoretical values, $\delta_1 = 1.721\sqrt{x\nu/U_\infty}$, $\delta_2 = 0.664\sqrt{x\nu/U_\infty}$ and $H = \delta_1/\delta_2 = 2.59$ of the Blasius boundary layer.

In order to extract an accurate wall-position, relative to the probe, from the experimentally measured profile a curve fitting method was employed. This

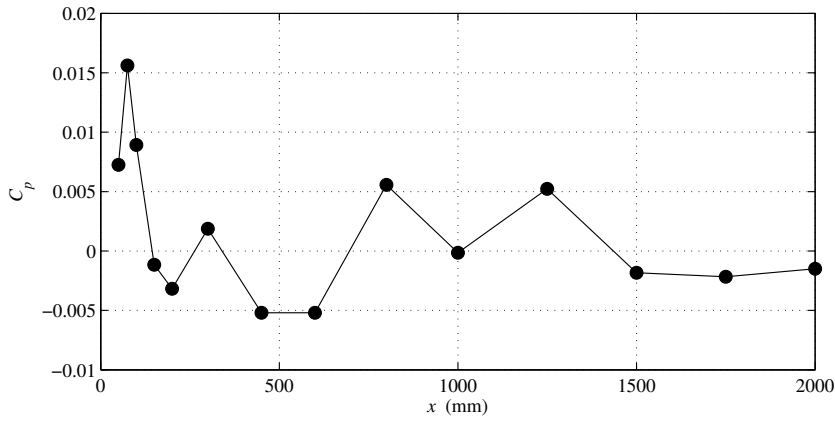


FIGURE 3.23. Pressure coefficient along x .

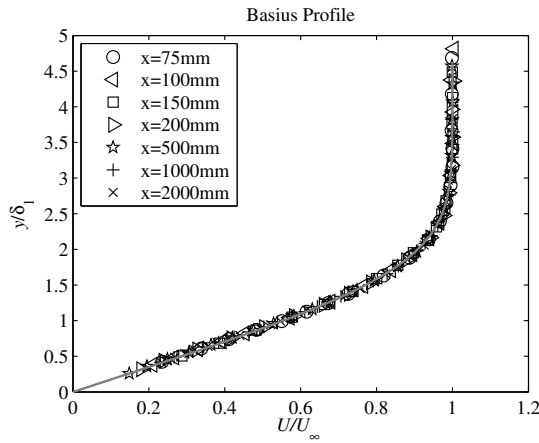


FIGURE 3.24. Mean velocity wall-normal profiles for different downstream locations from the leading edge. The solid line is the Blasius boundary layer profile.

method is described in Appendix A and is important if accurate integral length scales are to be calculated, since a small shift in the wall position will have a huge impact on the integral length scales (see e.g. Fransson (2001)). The method also allows for a good estimate of the skin-friction velocity independently of the user.

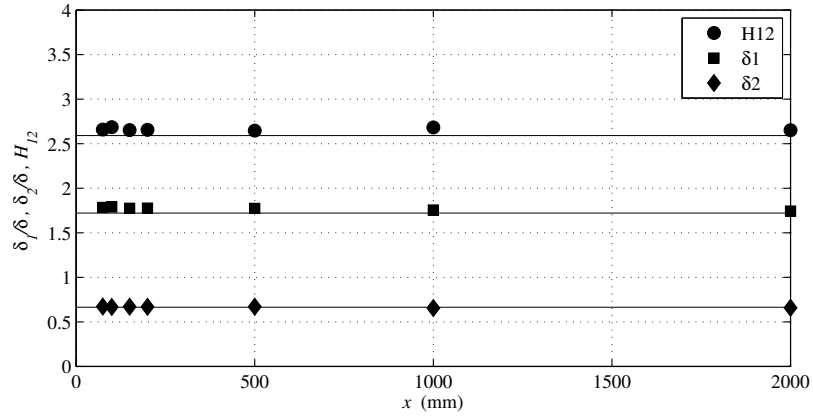


FIGURE 3.25. Shape factor, normalized displacement thickness and momentum thickness by $\delta = \sqrt{x\nu/U_\infty}$ along x . Solid lines show the theoretical values of the quantities.

Streamwise evolution of FST transitional boundary layer

All the measurements along the streamwise direction were carried out with two hot-wire probes separated in the spanwise direction. The following procedure was adopted:

- (1) A first coarse scan was performed in the streamwise and wall-normal directions for each case and the location of the u_{rms} -peak above the wall was identified.
- (2) At the u_{rms} -peak locations a two-point spanwise correlation measurement was performed in order to determine the spanwise location of maximum anti-correlation corresponding the half spanwise wavelength in average of the boundary layer streaks.
- (3) A fine scan was performed in the streamwise direction with the two probes separated with a distance corresponding to the averaged half spanwise wavelength of the streaky structures.

4.1. Intermittency

The intermittency can be estimated by analyzing the velocity signal. Here, the same method as proposed by Fransson *et al.* (2005) has been adapted. A brief summary of the method follows. First of all a cut-off frequency (f_{cut}) is defined and all the frequencies below that (laminar part of signal) is filtered away. In this investigation it is chosen as $f_{cut} = U_{\infty}/(4 \times \delta_{99})$, where δ_{99} is the thickness of Blasius boundary layer and hence a function of x . The next step is to define a threshold speed u_s and to set the filtered signal to zero below this threshold. The time ratio between the rest of the signal and the original one represents the intermittency (γ). In figure 4.1 the original velocity signal is shown along with the processed signal. For determining the threshold speed u_s in an objective way, a curve is produced depicting how the intermittency varies with u_s (see figure 4.2). The curve $\log(\gamma)$ vs u_s varies linearly for increasing u_s . The intermittency is defined as where this line crosses the vertical axis, in this example $\log(\gamma) \approx -0.97$ giving $\gamma = 0.38$ for $u_s \approx 0.016$ m/s.

With different FST characteristics different intermittency distributions are observed. The reason is mainly the different turbulence intensities at the leading edge. Figure 4.3 shows the intermittency distribution along the streamwise

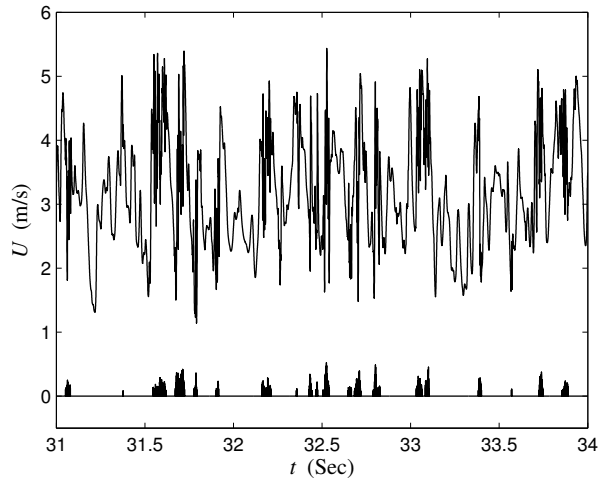


FIGURE 4.1. Typical velocity signal and filtered velocity signal. The intermittency is obtained as $\gamma = 0.38$

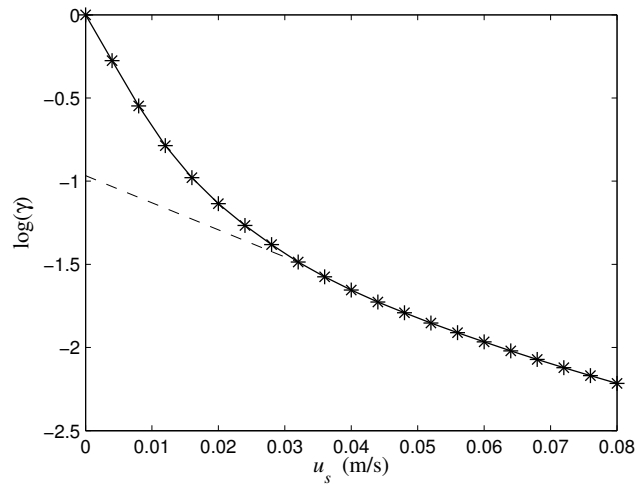


FIGURE 4.2. The symbols and solid line show the intermittency trend when the threshold varies. The dashed line shows how the real intermittency can be obtained.

direction for successively increasing turbulence intensity. As is shown, by increasing the injection (and so the turbulence intensity), transition occurs at a shorter distance from the leading edge and the length of the transition region becomes shorter.

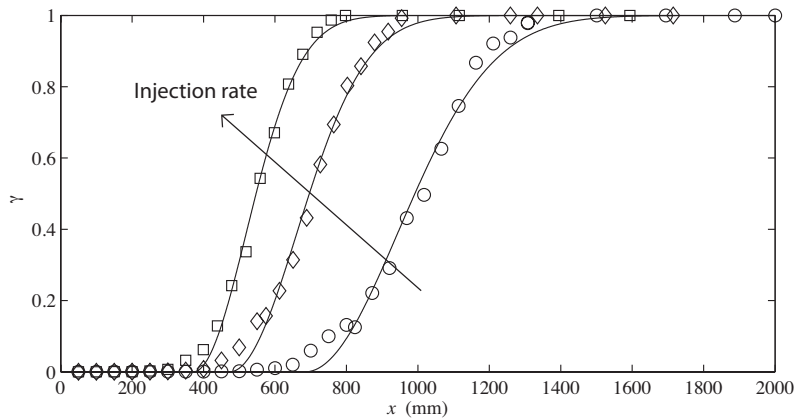


FIGURE 4.3. Typical intermittency distribution in the stream-wise direction. The three different cases represents three different injection rates for G1, which was located at 1400 mm in front of the leading edge.

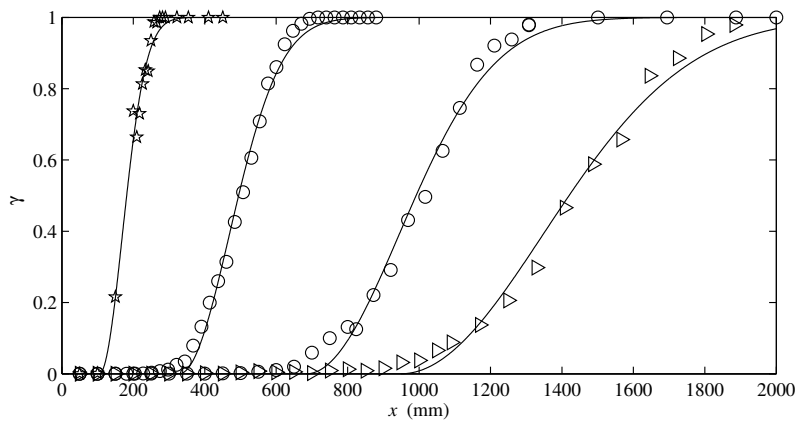


FIGURE 4.4. Typical intermittency distribution in the stream-wise direction. No injection has been applied here. Triangle and star symbols represent G7 and G8 mounted 1710 mm and 1000 mm before the leading edge, respectively. Circular symbols shows G1 mounted 800 mm and 1400 mm before the leading edge, respectively.

The range of transition regions would be even wider by considering different grids or different grid locations. Figure 4.4 presents the intermittency distribution for different grids without injection. One way to present all the

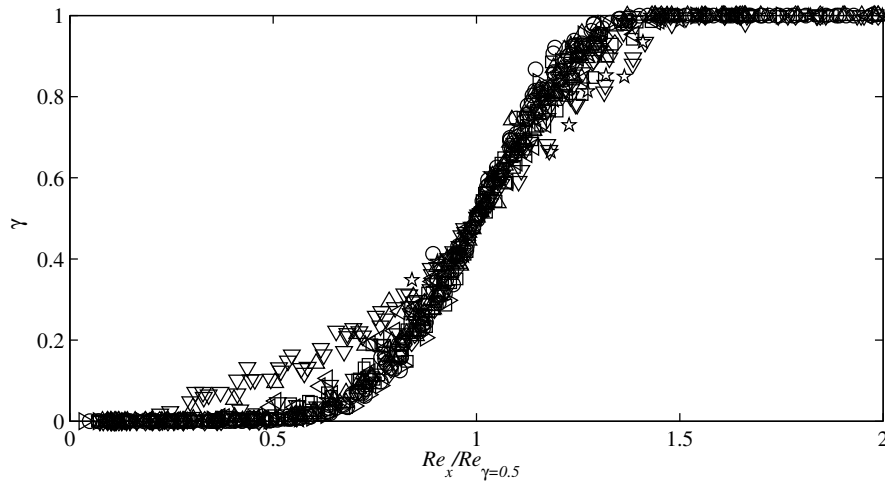


FIGURE 4.5. Intermittency trend in all the 42 cases. Streamwise distance is normalized by the location of $\gamma = 0.5$.

data is to normalize the Reynolds number with the Reynolds number where the intermittency (γ) is equal to 0.5. Figure 4.5 depicts such a normalization for all 42 cases. Although there is a good agreement between the data by the normalization, some scatter is observed and it is typically the high Tu cases which deviates.

A better way to normalize the streamwise coordinate is to introduce the non-dimensional coordinate (ξ). This ξ is defined as

$$\xi = \frac{x - x_{\gamma=0.5}}{x_{\gamma=0.9} - x_{\gamma=0.1}}. \quad (4.1)$$

If transition starts and ends at $\gamma = 0.1$ and $\gamma = 0.9$, respectively, and Re_{tr} is defined when $\gamma = 0.5$, then equation 4.1 can be written as $\xi = Re_x - Re_{tr} / \Delta Re_{tr}$, where ΔRe_{tr} is the transition region. Considering this new coordinate, the data shown in figure 4.5 show less scatter compared figure 4.6.

There have been many attempts to form the seemingly universal curve in figure 4.6. Johanson & Fashifar (1994) presented a relation for the curve as

$$\gamma(x) = 1 - \exp[-A(\xi + B)^3], \quad (4.2)$$

where A and B are constants. The best values for the constants by a curve fitting are 0.67 and 1.02, respectively. These values are comparable with the Fransson *et al.* (2005) results which were reported as 0.60 and 1.05, respectively.

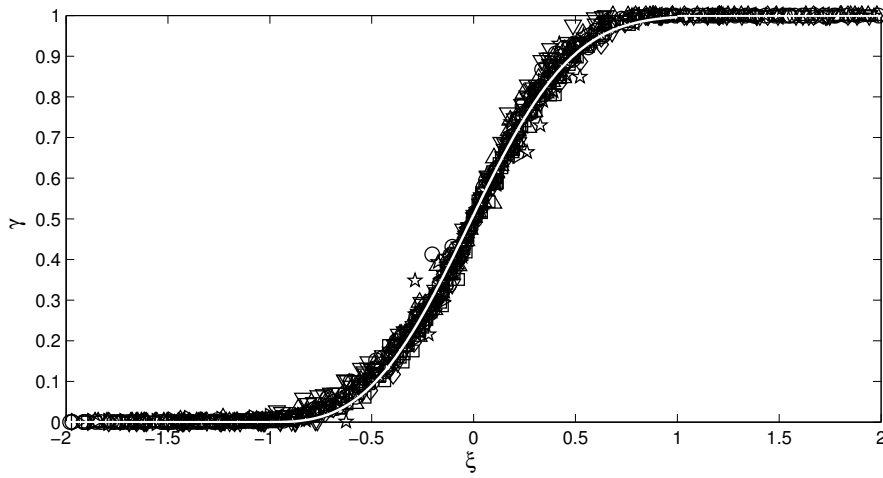


FIGURE 4.6. Intermittency distribution for all the 42 cases. Streamwise distance is normalized to ξ . The solid line shows the curve fit according to 4.2.

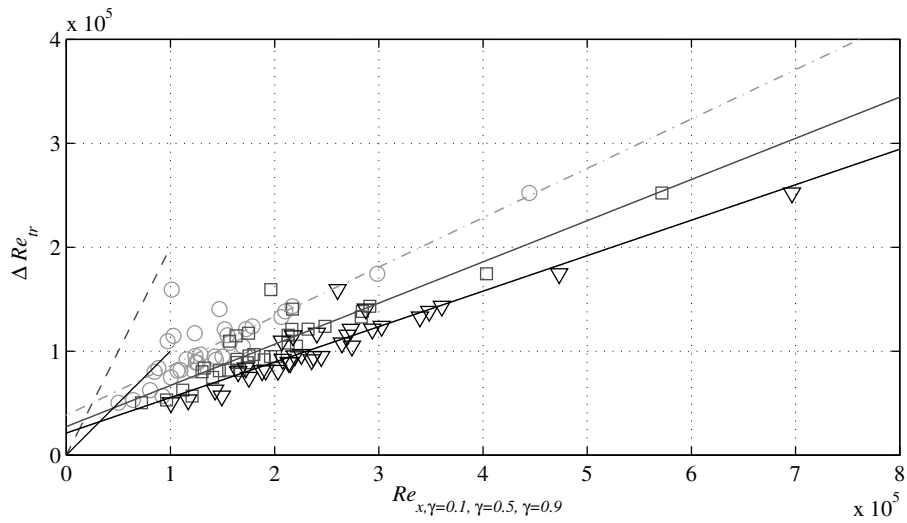


FIGURE 4.7. The relation between the length of transition and location of transition. Circles, squares and triangles represent intermittency of 0.1, 0.5 and 0.9, respectively.

4.2. Transition region

For employing the equation 4.2 or plotting figure 4.6, the length of the transition region (ΔRe_{tr}) and Re_{tr} are needed. For this purpose in each case the

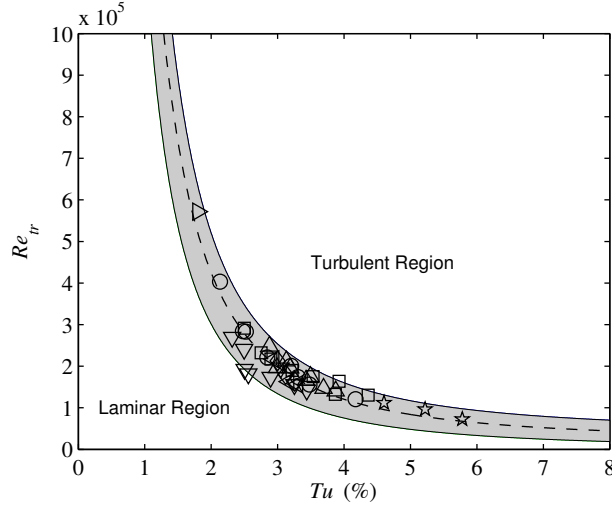


FIGURE 4.8. Transition region in dark. the symbols are the locations of $\gamma = 0.5$. The upper and lower solid lines correspond to $\gamma = 0.9$ and $\gamma = 0.1$ respectively. The dash line belongs to $\gamma = 0.5$.

location of the three different intermittency values ($\gamma = 0.1, 0.5, 0.9$) were determined through interpolation of the data. By knowing the location of $\gamma = 0.1$ and $\gamma = 0.9$ the length of the transition zone (ΔRe_{tr}) is obtained. Figure 4.7 shows the length of transition versus $Re_{\gamma=0.1,0.5,0.9}$. Circles, squares, and triangles represent intermittency of 0.1, 0.5 and 0.9, respectively, for all 42 cases. By passing straight lines through the data, the minimum possible length of the transition region corresponding to different $Re_{x,\gamma}$ can be obtained. It should be mentioned that there is a limitation for them. Even at high intensities, a minimum length is needed for the boundary layer to become turbulent. By assuming high turbulence intensity, the transition region starts at the leading edge so the length of transition region is either equal to the location where $\gamma = 0.9$ or to twice of the location where $\gamma = 0.5$. This assumption is shown in figure 4.7 with the solid and dashed lines passing the origin, corresponding to $Re_{minx,\gamma=0.9} = \Delta Re_{tr}$ and $Re_{minx,\gamma=0.5} = \Delta Re_{tr}/2$, respectively. The left hand sides of these lines are not allowed when considering above assumption. The crosses of these two lines with the solid black and solid gray lines (corresponding to empirical $Re_{x,\gamma=0.9}$ and $Re_{x,\gamma=0.5}$, respectively) provide two values of ΔRe_{tr} . In addition, the cross of dashed gray line ($Re_{x,\gamma=0.1}$) with the vertical axis ($Re_{x,\gamma=0.1}=0$) give another value of ΔRe_{tr} . These three ΔRe_{tr} are almost the same and have an average as $\Delta Re_{tr,min} = 4 \times 10^4$ and this equal to $Re_{minx,\gamma=0.9}$. This ΔRe_{tr} gives also $Re_{minx,\gamma=0.5} = 2 \times 10^4$.

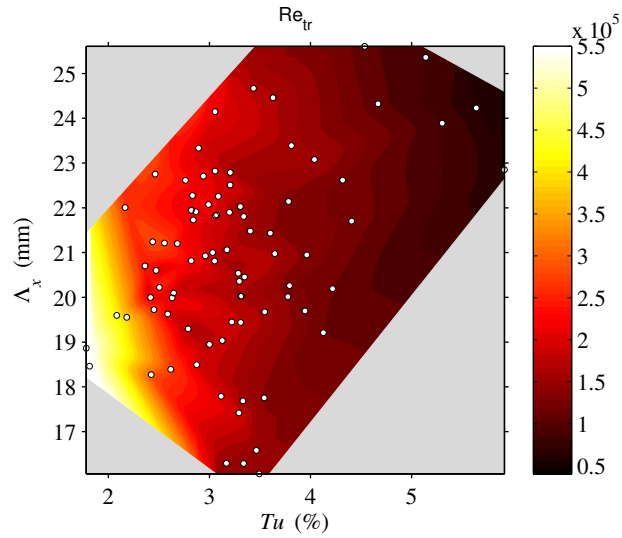


FIGURE 4.9. Re_{tr} filled contour plot based on the turbulence intensity (Tu) and integral length scale (Λ_x) at the leading edge.

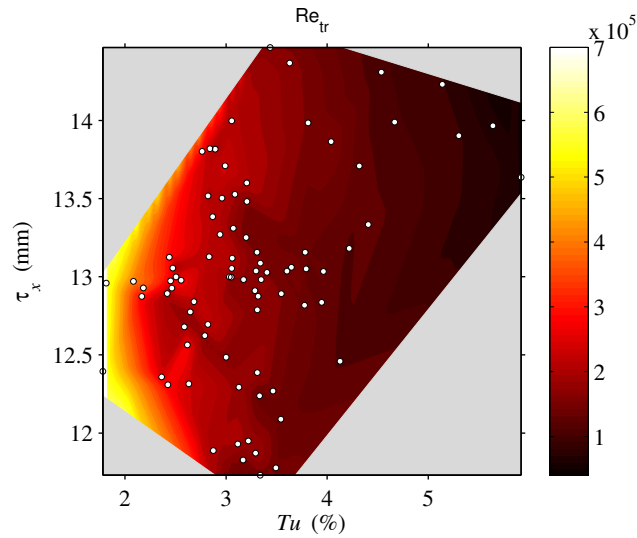


FIGURE 4.10. Re_{tr} filled contour plot based on the turbulence intensity (Tu) and Taylor length scale (τ_x) at the leading edge.

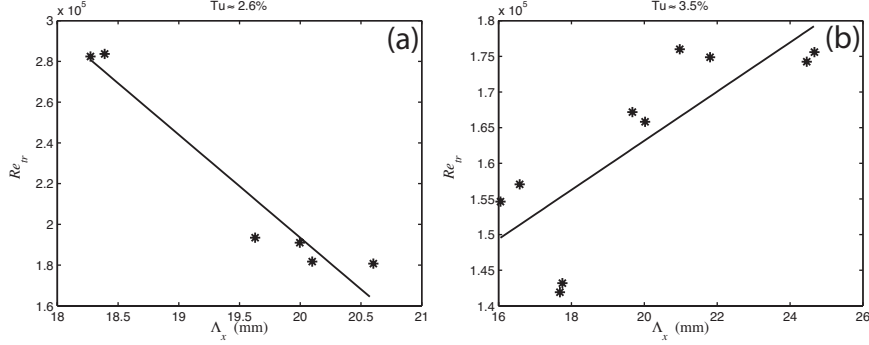


FIGURE 4.11. Re_{tr} distribution when the Λ_x varies at $Tu \approx 2.6\%$ (a) and $Tu \approx 3.5\%$ (b).

Assuming that when the energy inside the boundary layer reaches a certain amount, the streaks break-down to turbulent spots, lead to the point that the transition location is a function of the input energy, (i.e. the turbulence intensity at the leading edge Tu_{LE}). By considering the minimum receptivity distance, the relation between transition location and intensity at the leading edge can be written as

$$Re_{x,\gamma} = C_\gamma \cdot Tu^{-2} + Re_{\gamma,\min} , \quad (4.3)$$

with the exponent of -2 on Tu coming from the argumentation used in Andersson *et al.* (1999). C_γ is 1.20×10^4 , 1.62×10^4 and 1.92×10^4 , respectively, for $\gamma = 0.1$, $\gamma = 0.5$ and $\gamma = 0.9$, respectively. By knowing these coefficients, it is possible to estimate the transition region. Such a region is shown in figure 4.8. The symbols depict the transition location ($\gamma = 0.5$). This figure reveals that by increasing the intensity at the leading edge, the transition occurs closer to the leading edge but with a limitation. In addition, at lower turbulence intensities ($Tu < 1\%$) the transition occurs far away from the leading edge.

The transitional Reynolds number (Re_{tr}) can be evaluated based on integral length scale (Λ_x) and Taylor length scale (τ_x) at the leading edge. As shown in figures 4.9 and 4.10 the main factor which affects the Re_{tr} is turbulence intensity at the leading edge (Tu).

By focusing on a constant Tu (practically narrow band of Tu), one can see the trend of transition location. Figure 4.11 shows the distribution of transition location (Re_{tr}) while the integral lengthscale (Λ_x) changes at constant Tu . As seen in 4.11 (a), at a chosen low turbulence intensity ($Tu = 2.6 \pm 0.1\%$), by increasing (Λ_x), the transition occurs at lower streamwise distance from the leading edge. On the other hand, at a chosen high turbulence intensity

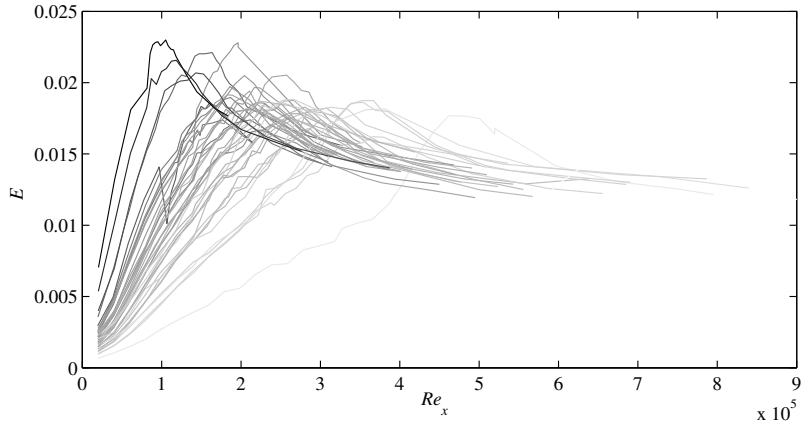


FIGURE 4.12. Energy growth in the boundary layer. The darker line the higher turbulence intensity at the leading edge.

($Tu = 3.5 \pm 0.1\%$), there is a delay in transition by increasing Λ_x (figure 4.11 b). Note, the effect of Λ_x on transition is higher at low Tu . The derivation of transition location ($dx_{tr}/d\Lambda_x$) for low and high Tu is -125 and $+8$, respectively. Jonas *et al.* (2000) and Nagarajan *et al.* (2007) reported the transition location moves downstream with increasing the free-stream lengthscale both at $Tu=3\%$.

4.3. Streamwise evolution of second and higher order velocity moments

Besides the intermittency, the velocity moments and their streamwise evolution have been evaluated. Recall all measurements were taken at the wall-normal location of maximum u_{rms} . u_{rms} , skewness and flatness are the second to fourth order of moments, but in this study the normalized energy was evaluated instead of the second order moment.

By defining $E = (u_{rms}/U_\infty)^2$ it is possible to show the growth of energy in the boundary layer as done in figure 4.12. The general energy distribution in the streamwise direction shows an energy peak at some downstream location followed by a decay towards an asymptotic level of the energy around 0.0012. The higher the input energy (i.e. higher intensity at the leading edge) moves the peak closer to the leading edge and makes the peak more energetic. This peak location seems to correspond to the point where streaks have broken-down to turbulence spots and now are merging. By using the normalized distance from the leading edge (ξ), the peak locations confirm this statement. Figure 4.13 reveal the normalized energy distribution versus of ξ . As seen, all the energy peaks collapse almost around $\xi = 0.50$ which corresponds to $\gamma = 0.9$. This

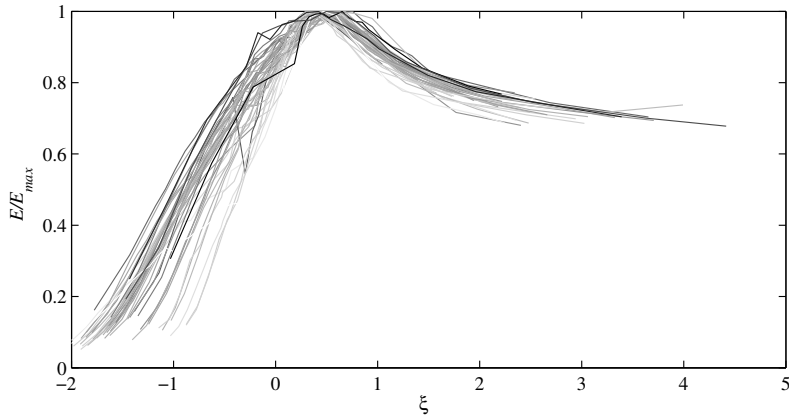


FIGURE 4.13. Normalized energy distribution in the boundary layer versus ξ . The darker line the higher turbulence intensity at the leading edge.

shows that in all cases, the energy reach a maximum value at the end of the transition region before the boundary layer becomes fully turbulent.

Figure 4.14 shows the disturbance growth ($G = dE/dRe_x$) in the energy interval $0.0025 < E < 0.0115$. This is the same definition of G as in Fransson *et al.* (2005) but with the upper limit reduced to 0.0115 from 0.0125. The reason is the clear onset of an increased growth rate from the lowest turbulence intensity case. The data is plotted versus the inlet energy of the streamwise as well as the vertical velocity components, Tu^2 and Tv^2 , respectively. The growth rate increases linearly with the inlet FST energy in the free-stream. In the vertical component the growth rate is somewhat higher since the anisotropy measure v_{rms}/u_{rms} is always below unity.

Skewness and flatness are two quantities which were evaluated. Figure 4.15 shows the evolution of skewness for all cases. As observed, the skewness decrease to become negative prior to the transition onset, i.e. in the region $\xi < -0.5$. Having reached the location of transition onset the skewness increase rapidly and become positive with a positive peak somewhat after the mid transition ($\xi = 0$), and again becomes negative in the turbulent region, $\xi > 1$.

In all cases they have same trend, which are illustrated for two cases in figures 4.16 and 4.17. As can be seen, $\xi \approx -0.5$ and $\xi \approx 0.5$ (corresponding to $\gamma \approx 0.1$ and $\gamma \approx 0.9$) have a major role in the skewness distribution. This quantity starts to increase at $\xi \approx -0.5$ and after a peak at $\xi \approx 0.0$ ($\gamma \approx 0.5$) it decays and saturates to constant value after $\xi \approx 0.5$ where the boundary layer becomes turbulent. Furthermore, the flatness peak moves toward the

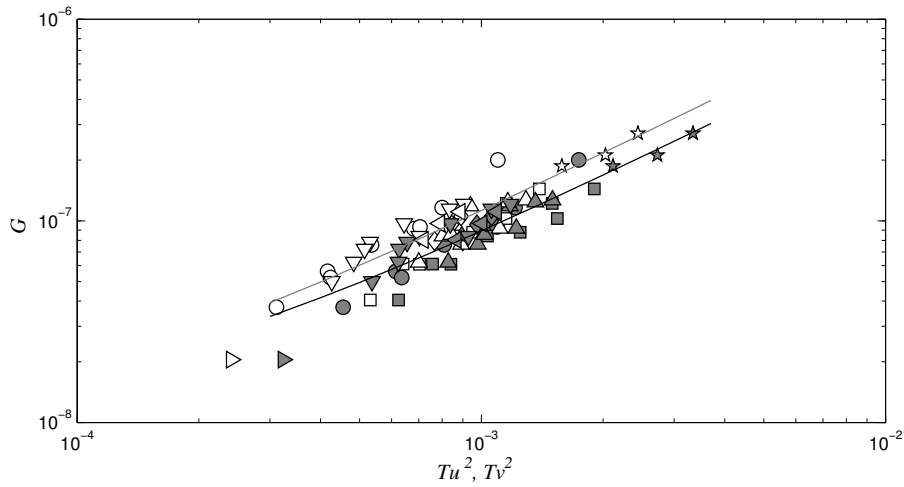


FIGURE 4.14. Linear energy growth versus input energy. The darker and lighter symbols and lines show the energy growth versus Tu^2 and Tv^2 , respectively.

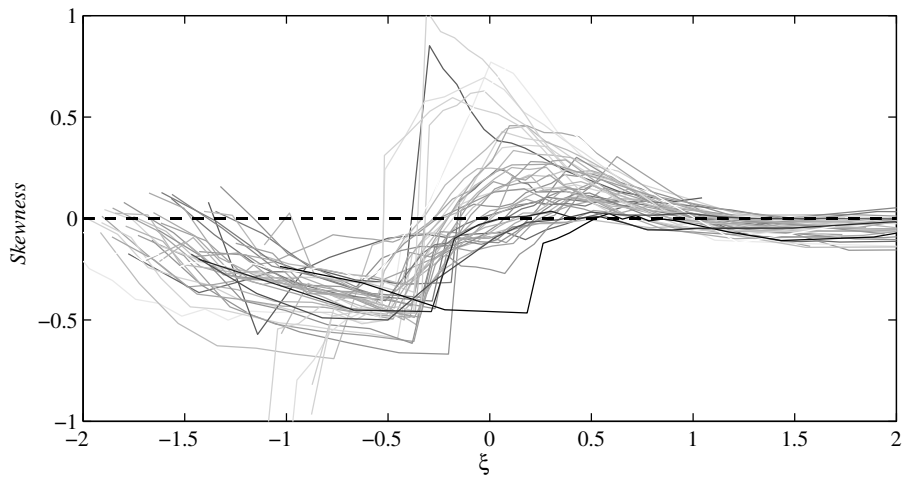


FIGURE 4.15. Skewness versus ξ for all cases. The darker lines mean higher turbulence intensity at the leading edge.

lower streamwise direction with higher turbulence intensity. The energy distributions are slightly different. In low turbulence intensity, the increasing slope of the curve change around $\xi \approx -0.2$ which is not observed in high turbulence

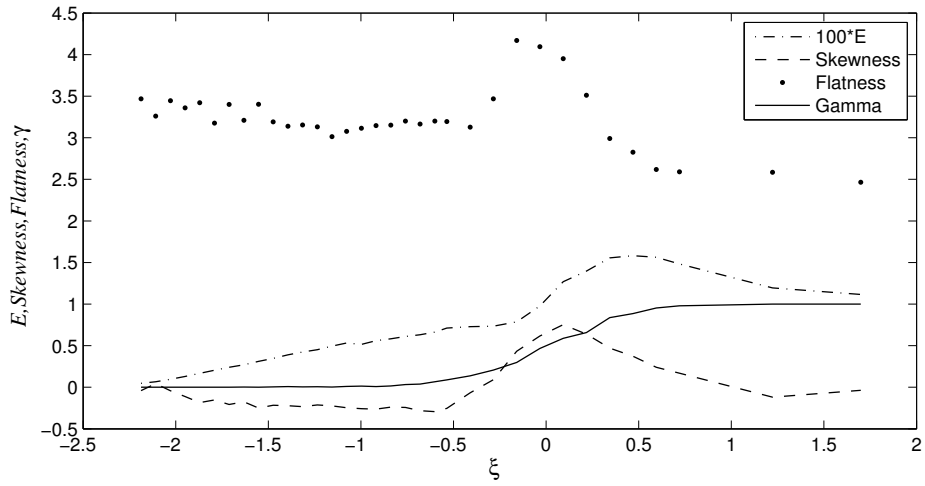


FIGURE 4.16. Energy, skewness, flatness and γ versus ξ for a typical case: G7 located at 1710 mm before the leading edge and without secondary flow injection.

intensity. It may be hypothesized that the slow energy growth for low Tu -levels is by-passed at high Tu -levels because of a much higher activity of the streaks.

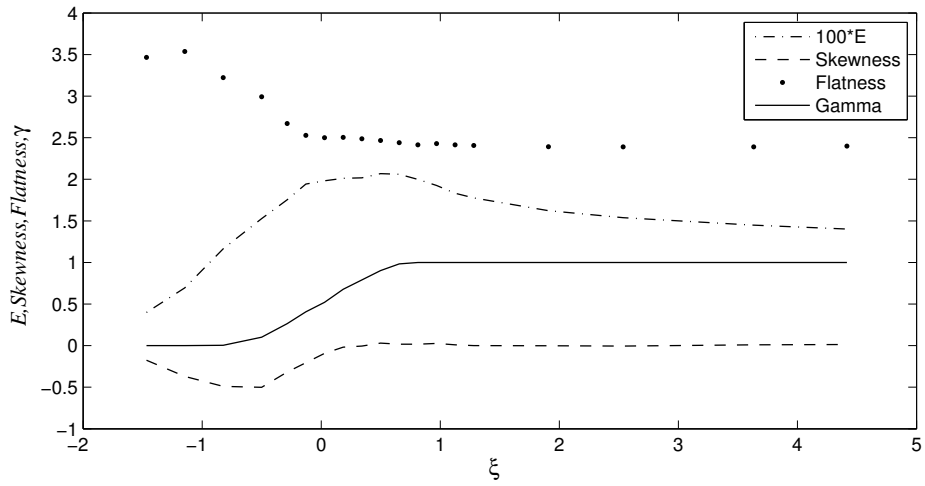


FIGURE 4.17. Energy, skewness, flatness and γ versus ξ for a typical case: G8 located at 1400 mm before the leading edge and without secondary flow injection.

Wall-normal profiles in transitional boundary layers

For evaluating the velocity moments and the intermittency in the wall-normal direction, five downstream positions from the leading edge were chosen and the measurements were carried out in those locations. These X-positions cover the laminar, the transition and the turbulent region. Note, all profiles were measured simultaneously with two hot-wire probes separated by a distance corresponding to the averaged half spanwise wavelength of the streaky structures inside the boundary layer. Boundary layer parameters and friction velocities presented in this chapter were calculated using the method described in Appendix A.

5.1. Streamwise evolution of mean velocity profiles

Figure 5.1 shows mean velocity wall-normal profiles for all cases in different locations. The darker lines correspond to higher intermittency (γ) as it is shown on the colorbar in percentage. In this picture the horizontal axis corresponds to the normalized velocity by free stream velocity (U_∞) and the vertical axis shows the wall normal position normalized by the displacement thickness (δ_1). As observed, the profiles change gently from the Blasius profile (lightest line, $\gamma = 0\%$) to a turbulent profile (darkest line, $\gamma = 100\%$). For a specific case the increase in darker would correspond to an increased downstream distance from the leading edge.

Another way to normalize the data is to use the friction velocity u_τ and the viscous length scale (l^*), respectively, according to

$$u_\tau = \sqrt{\frac{\tau_w}{\rho}} \quad (5.1)$$

and

$$l^* = \frac{\nu}{u_\tau} . \quad (5.2)$$

This inner scaling is used for the second order velocity moments as well as for the streaky structure lengthscale.

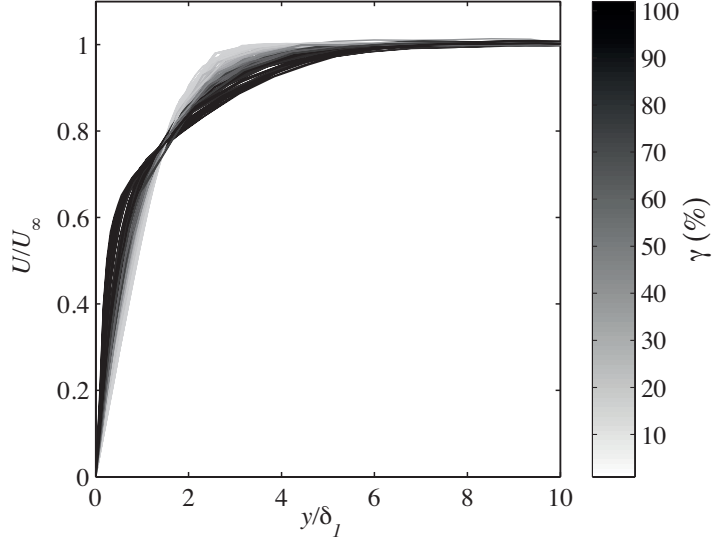


FIGURE 5.1. Mean velocity profiles for all cases. The color bar shows intermittency (γ).

5.2. Integral quantities

The *displacement thickness* (δ_1) and *momentum thickness* (δ_2) are integral quantities of the mean velocity profile and change in the streamwise direction when the boundary layer becomes intermittent. In this section these quantities as well as their ratio $H = \delta_1/\delta_2$ were calculated from the data measured in the wall normal direction. Figure 5.2 depicts normalized displacement and momentum thicknesses with δ ($= \sqrt{x \cdot \nu / U_\infty}$). For a better description, the horizontal axis is considered as ξ instead of x which sorts the data in the transition region.

In figure 5.2 one may observe that the measured data agrees nicely with the theoretical Blasius values ($\delta_1/\delta = 1.721$, $\delta_2/\delta = 0.664$ and $H_{12} = 2.59$) for $\xi < -1$. After $\xi \approx -1$, δ_1/δ stays constant around the theoretical value while δ_2/δ increases, reflecting a change into a fuller profile as compared to Blasius. Consequently, the shape factor decreases. The constant δ_1/δ may be explained by an equal amount of velocity excess close to the wall (fuller profile) as velocity deficit further away from the wall. This may be observed in figure 5.1. Note that the shape factor for a fully turbulent boundary layer is typically around 1.3, meaning that the present turbulent boundary layer profile with a shape factor 1.5 at the lowest are still developing.

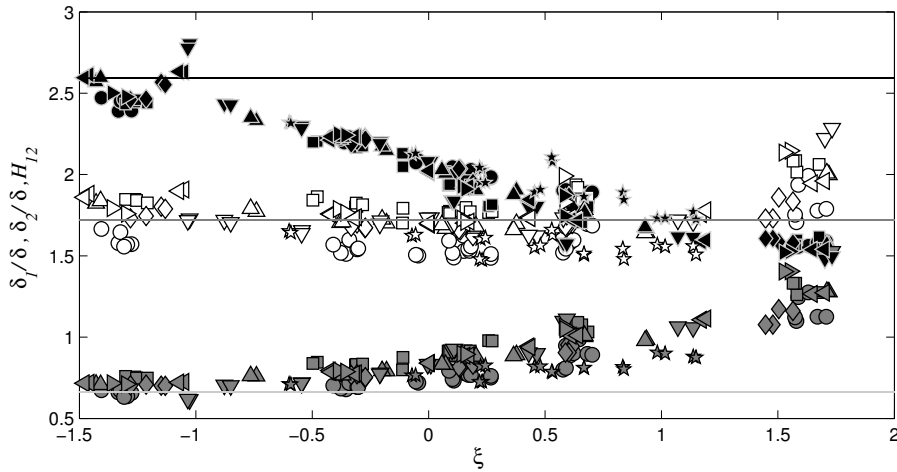


FIGURE 5.2. Integral quantities and their variation in the streamwise ξ -direction. The solid lines shows the Blasius results for the displacement thickness ($\delta_1/\delta = 1.721$), the momentum thickness ($\delta_2/\delta = 0.664$) and the shape factor ($H_{12} = 2.592$).

5.3. Friction coefficient

The wall-normal measurements were employed to calculate the friction coefficients in the streamwise direction. Figure 5.3 presents the evolution of the friction coefficient $c_f = \tau_w / \frac{1}{2} \rho U_\infty^2$. Besides the symbols showing the 42 FST cases, the (\times)-symbols depict the laminar case without any grid in the wind tunnel. The dashed and dash-dotted lines show the theoretical and empirical lines of c_f for the laminar and the turbulent regions, respectively, corresponding to

$$\begin{aligned} c_{f,lam} &= 0.664^2 Re_\theta^{-1}, \\ c_{f,turb} &= 2[1/0.38 \log(Re_\theta) + 4.08]^{-2}. \end{aligned} \quad (5.3)$$

The darker symbols correspond to higher intermittency (γ) and are obviously closer to the turbulent dash-dotted line. In order to have a better view of the trend, few cases were selected and plotted in figure 5.4. In this figure the colors show the turbulent intensity in the free-stream at the leading edge and the cross symbols shows the case without any grid. Naturally, all the cases start with a laminar boundary layer and the data almost lies on the dashed laminar curve. By increasing the distance from the leading edge, the curves start to deviate from laminar curve and enters the transitional zone. As the turbulence

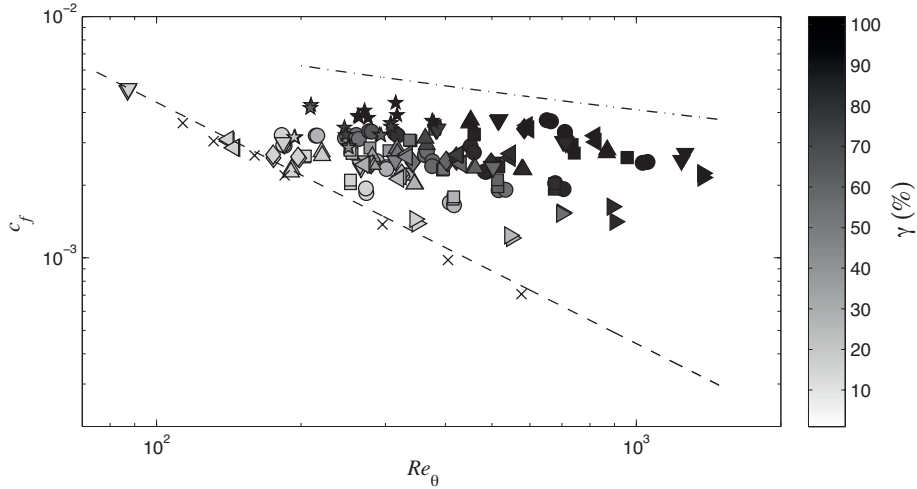


FIGURE 5.3. Friction coefficient variation in the streamwise direction. Re_θ is defined based on momentum thickness (δ_2). The cross symbols are the case without any grid and so very low turbulent intensity in the free stream. The darker symbols correspond to higher intermittency (γ). The dashed and dash-dotted lines show the empirical laminar and fully turbulent coefficients, respectively.

intensity increases this deviation happens at lower Re_θ . For instance, while G7 with intensity of $Tu \simeq 1.8\%$ starts to deviate from the dashed line at $Re_\theta \simeq 350$, G5 located 100 mm before the leading edge with intensity of $Tu \simeq 3.0\%$ starts departing from the laminar pattern already at $Re_\theta \simeq 100$. Again it can be noted, just as with H_{12} , it seems that the last points of the curves do not lay on the empirical turbulent line. This, because of the fact that the last points are not taken in a fully developed turbulent boundary layer.

5.4. Intermittency distribution in the wall-normal direction

The intermittency calculation method which was described in 4.1 is the same for calculating the intermittency along the wall-normal direction but with a different cut-off frequency. The cut-off frequency $f_{cut} = U_\infty / (4 \times \delta_{99})$ is valid just inside the boundary layer and does not support the reality at the edge and outside of the boundary layer with the presence of free-stream turbulence, i.e. $\gamma = 1$. So, a Heaviside function was introduced to correct the cut-off frequency as,

$$H(y) = 1 + \frac{1}{1 + e^{-a \cdot (y/\delta_{99}) + b}}. \quad (5.4)$$

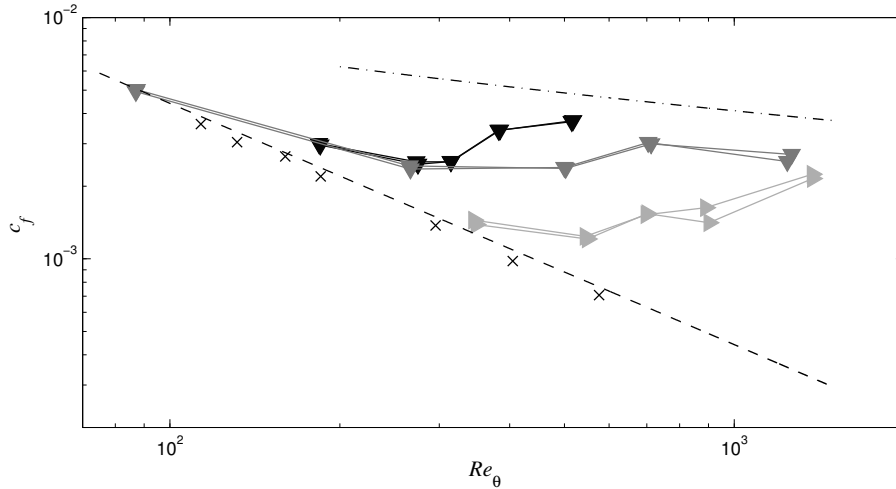


FIGURE 5.4. Friction coefficient variation in the streamwise direction. Re_θ is defined based on momentum thickness. The cross symbols are the case without any grid and so very low turbulent intensity in the free-stream. The darker symbols correspond to higher intermittency (γ). The dashed and dash-dotted lines show the theoretical laminar and the empirical turbulent coefficient.

In this equation the coefficients a and b were both chosen to be 44. These values make the function vary from 1.1 to 1.9 in the range of $0.95 < y/\delta_{99} < 1.05$, where δ_{99} correspond to the boundary layer thickness. So, the final cut-off frequency can be written as

$$f_{cut}(x, y) = \frac{U_\infty}{4 \times \delta_{99}(x)} \left(1 + \frac{1}{1 + e^{44(1-y/\delta_{99}(x))}} \right), \quad (5.5)$$

where y is the wall-normal distance and δ_{99} is Blasius boundary layer thickness at a certain distance x from the leading edge. By such a cut-off frequency, all wall-normal measurements of γ can correctly be presented as in figure 5.5.

In figure 5.5, the colorbar shows the ξ -coordinate based on the intermittency γ at the wall distance where the u_{rms} is maximum. As can be seen, at lower ξ :s the intermittency is zero ($\gamma = 0$) inside the boundary layer and after a jump at the edge of boundary layer, the intermittency become one in the free-stream. On the other hand, at higher ξ , the intermittency is almost the same (except for narrow region close to the wall) as the intermittency in the free-stream, i.e. $\gamma = 1$. In addition, in the transition zone, the intermittency

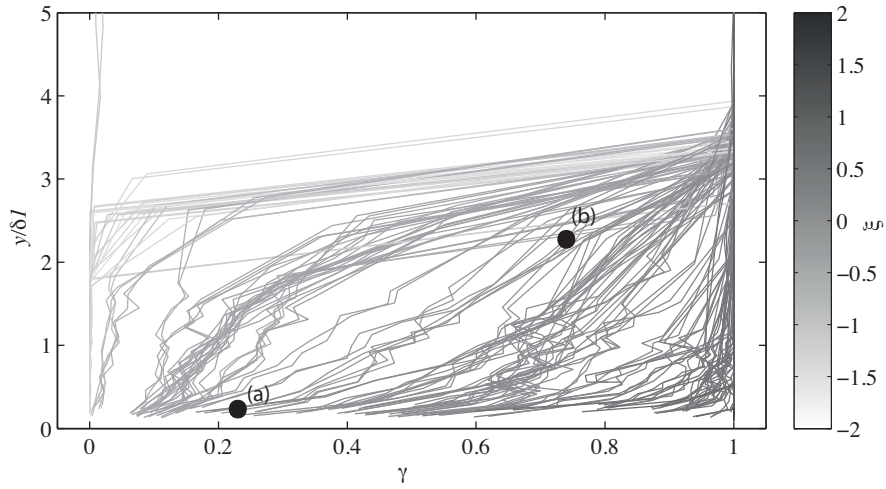


FIGURE 5.5. Intermittency in both x and y direction. Instead of x the normalized coordinate ξ is used as color bar

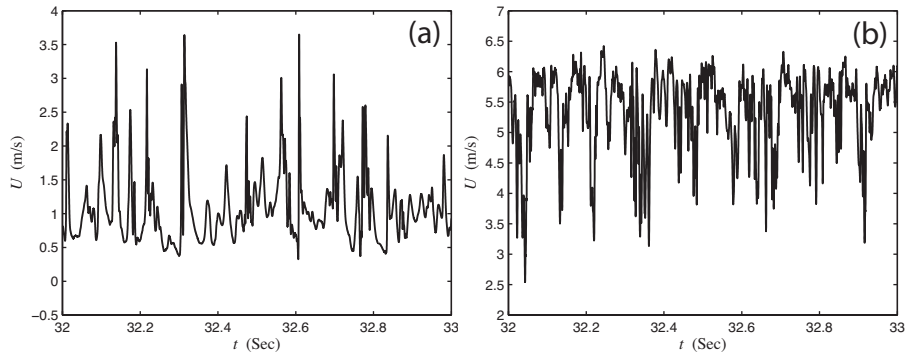


FIGURE 5.6. Signals at different wall-normal position in the transition region ($G1$, $X_{grid}=800$ mm, $Injection_{max}$, $x - x_L = 298$ mm). (a) and (b) correspond to the marked points in figure 5.5.

changes in the boundary layer to become the same as in the free-stream. Figure 5.6 shows two signals in one case. The difference between the intermittency inside the transitional boundary layer can be seen easily.

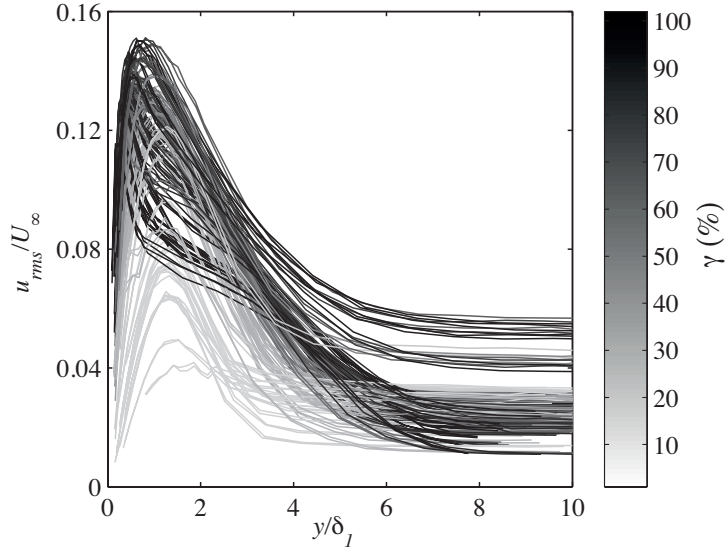


FIGURE 5.7. The wall normal distribution of normalized u_{rms} .

5.5. Higher order velocity moments

The second order moment u_{rms} were measured at different distances from the leading edge along the wall-normal direction. Figure 5.7 depicts the distributions of normalized u_{rms} versus normalized y . The colorbar shows the intermittency in percentage. It seems that, at higher γ -value the peak values of u_{rms} increases while the location of the maximum value move towards the wall. Figure 5.8 shows the same trend but sorted in different ξ intervals.

For an even better view figure 5.9 shows the maximum u_{rms} versus y position. Obviously, the location of maximum u_{rms} becomes closer to the wall when the boundary layer enters the transition region and finally the turbulent region. On the other hand, the maximum u_{rms} has a peak when the flow becomes intermittent and after that there is a decreasing trend.

Another way to normalize the second order moment is with the inner scales (u_{τ} and l^*). Figure 5.10 present such a graph and the maxima are shown in figure 5.11. The evolution of the maxima with increasing γ is somewhat more complicated in plus-unit. One may observe that the $\max\{u_{rms}^+\}$ is around $y^+ = 20$ for low intermittency and that it moves away from the wall in plus-unit as γ increases. Having past γ above 50% the disturbance peak move toward $y^+ = 15$, which is the location in a fully turbulent boundary layer.

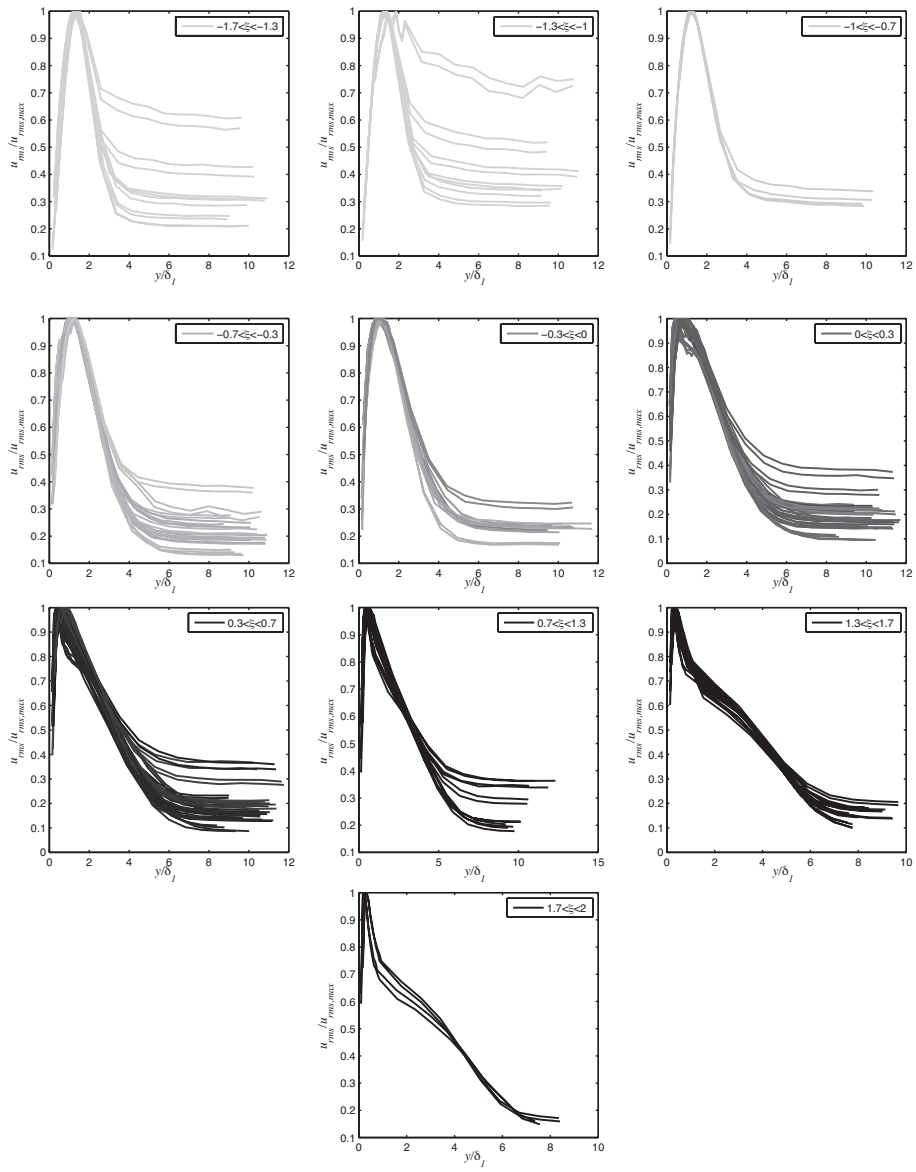


FIGURE 5.8. u_{rms} at different ξ .

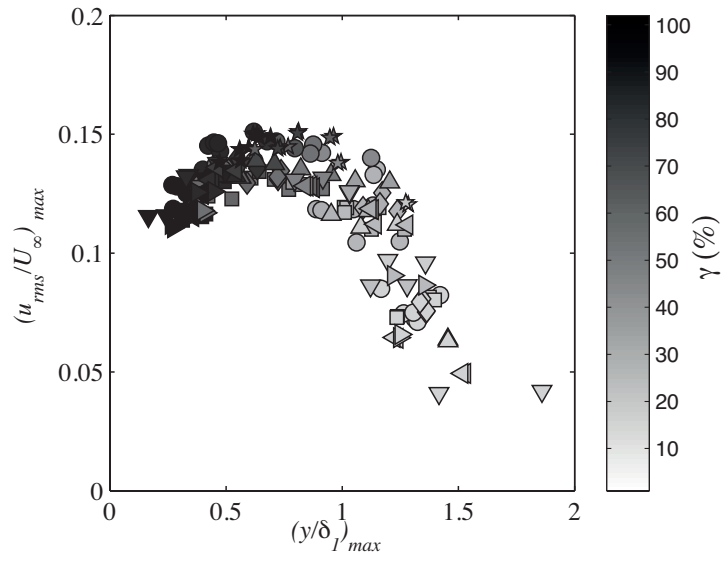


FIGURE 5.9. The evolution of maximum disturbance versus the position.

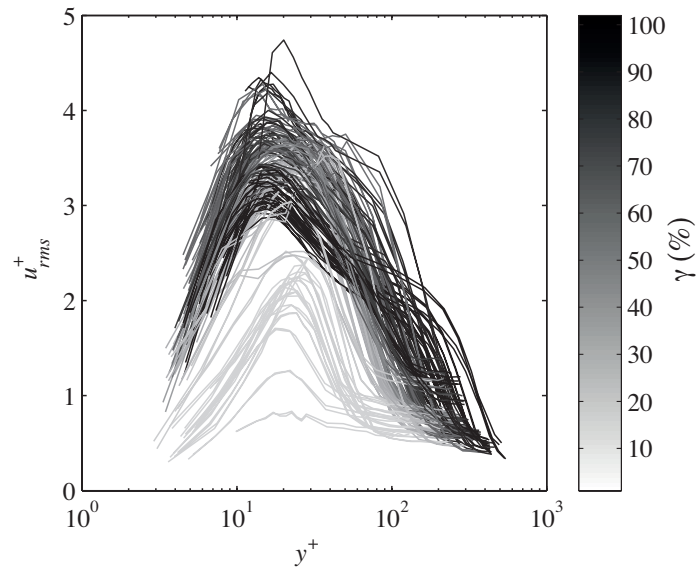


FIGURE 5.10. Normalized the second order moment and wall normal distance by u_{τ} and l^* .

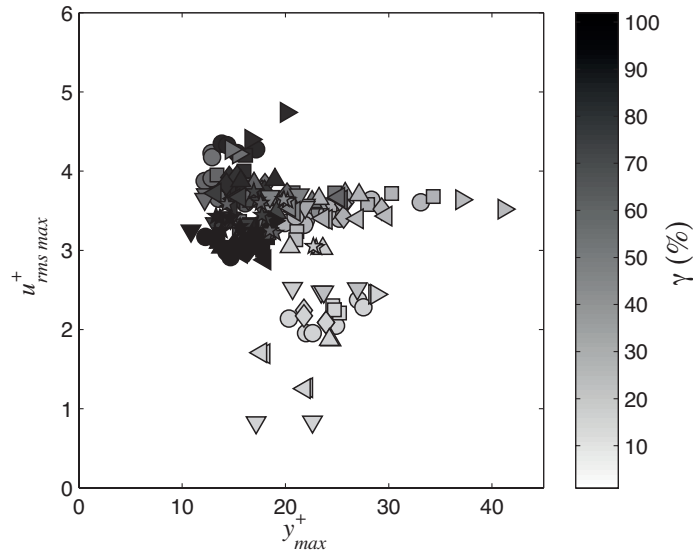


FIGURE 5.11. The evolution of maximum disturbance versus the position in the scale of u_{τ} and l^* .

Figures 5.12 and 5.13 show the skewness and flatness in the wall-normal direction for all cases. For a cleaner view, by choosing a typical case (G3, $X_{grid} = -1300$ mm and Injection MAX) the trend of these moments are shown in figures 5.14 and 5.15 with increasing downstream distance corresponding to an increase in γ . As it can be seen, there is a negative and positive in skewness and flatness, respectively, around the boundary layer edge. Close to the wall the velocity is positively skewed.

5.6. Two-point correlation

Another quantity which was analyzed is the spanwise correlation. The measurements were performed in the wall-normal direction. Figure 5.16 shows the trend of R_{uu} in all cases. A comparison between the position of maximum u_{rms} and minimum cross-correlation is depicted in figure 5.17. It seems that at lower intermittency the maximum u_{rms} occurs above the minimum cross-correlation, but they become closer to each other and even minimum cross-correlation happens on top of the u_{rms} .

Another way to look at the evolution of R_{uu} is to consider it in xy -plane. In figure 5.18 the dimensionless x coordinate (ξ) is used to show streamwise development. As can be seen the maximum anti-correlation moves towards the wall and becomes weaker at the same time.

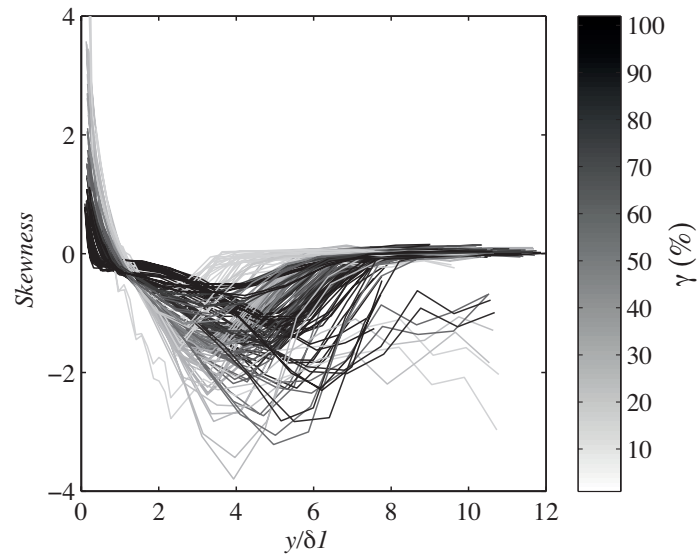


FIGURE 5.12. The 3rd order moment vs wall normal distance.

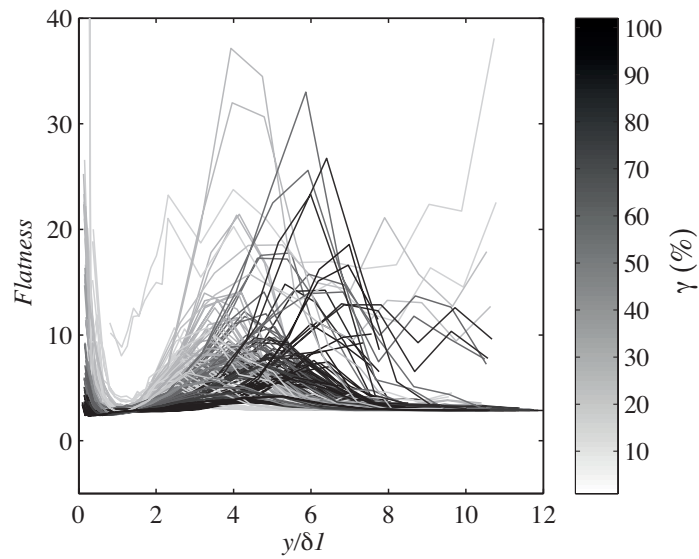


FIGURE 5.13. The 4th order moment vs wall normal distance.

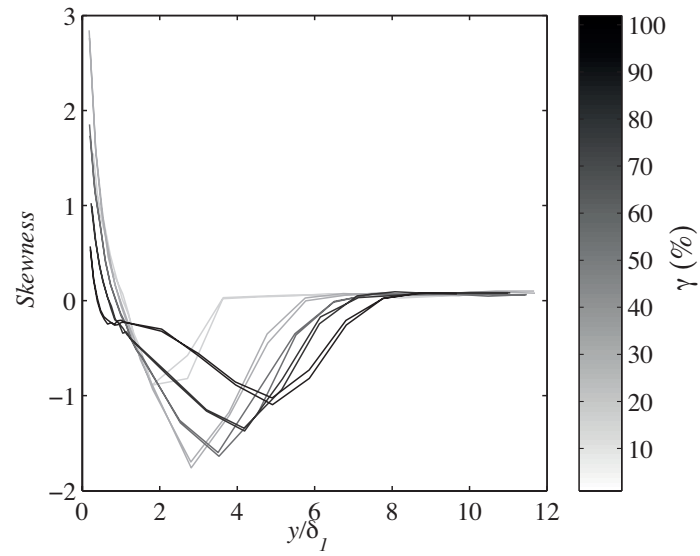


FIGURE 5.14. The 4th order moment and wall normal distance.

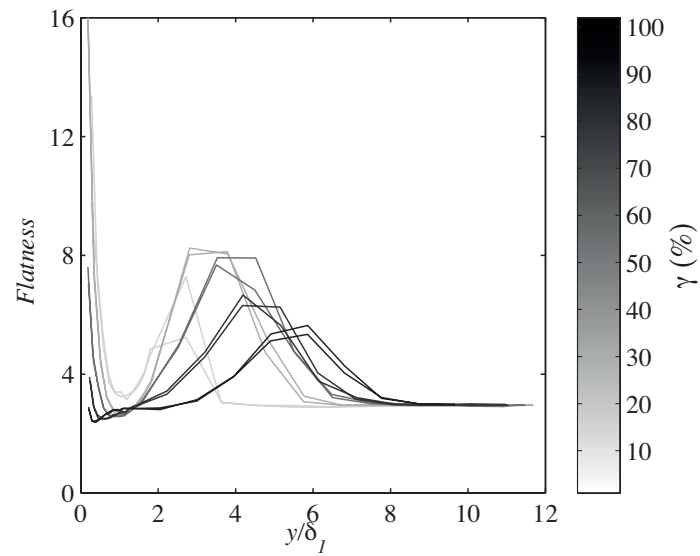


FIGURE 5.15. The 3rd order moment and wall normal distance.

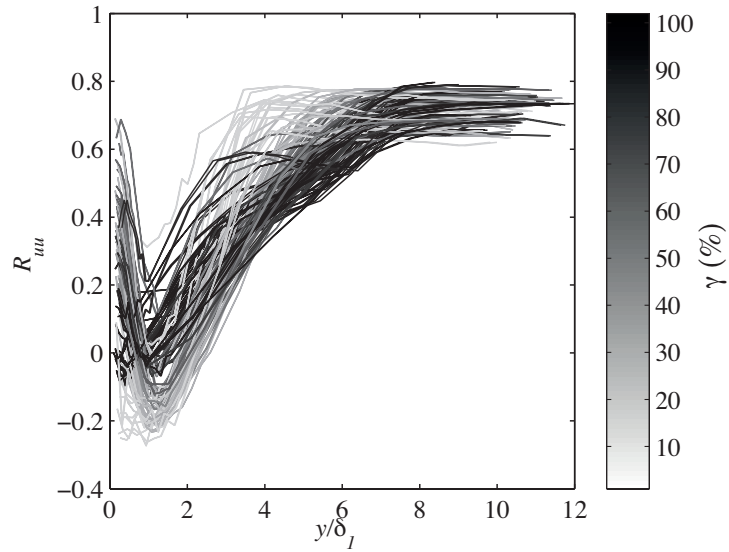


FIGURE 5.16. The spanwise two-point velocity correlation in the wall-normal direction.

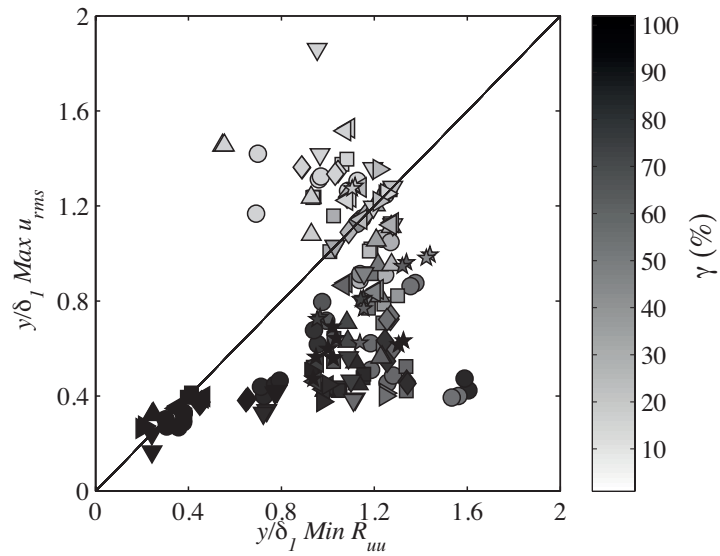


FIGURE 5.17. The maximum anti spanwise correlation location versus the maximum u_{rms} in wall normal direction.

5.7. Probability Density Function

The evaluated velocity probability density function (PDF) in a typical case (Grid 4, $X_{grid} = -1400\text{mm}$ and without injection) is depicted in figure 5.19. The colors which correspond to two hot wires show a good agreement with each other. For a better view instead of wall normal direction (y), the velocity is shown. Obviously, in all cases the PDF in the free-stream ($U_\infty = 6\text{ m/s}$) have the same pattern. On the other hand, the evolution of PDF inside the boundary layer is strong. Really close to the wall ($U < 1\text{ m/s}$), the peak of the PDF is very narrow but decrease and becomes wider as ξ increases. This means that the disturbances reach an asymptotic state when the boundary gets turbulent. At the middle of the boundary layer ($1 < U < 5\text{ m/s}$), the PDF curves are symmetric in the laminar region ($\xi < -0.5$). As entering transition and fully turbulent region $\xi > -0.5$, the curves start to decline: near the wall they tend to have a high speed tail and near the edge of boundary layer have a low speed tail corresponding to the positive and negative skewness as discussed previously. This behavior shows mixing phenomenon in transition and turbulent region.

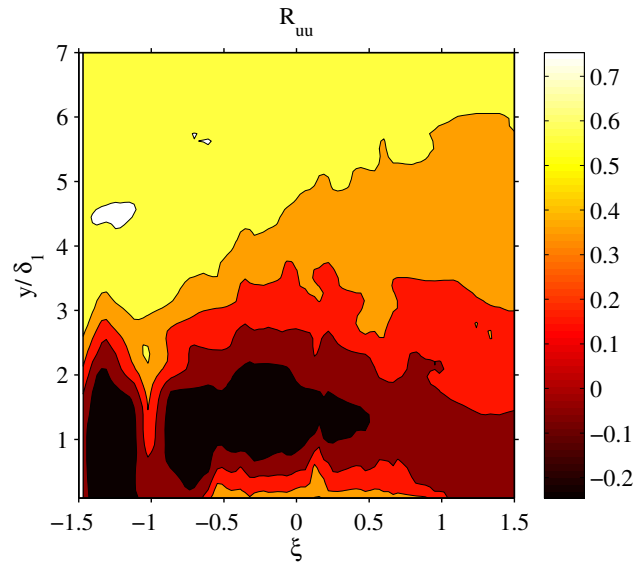


FIGURE 5.18. The filled contour plot of spanwise cross correlation in the xy -plane. Both axes are normalized.

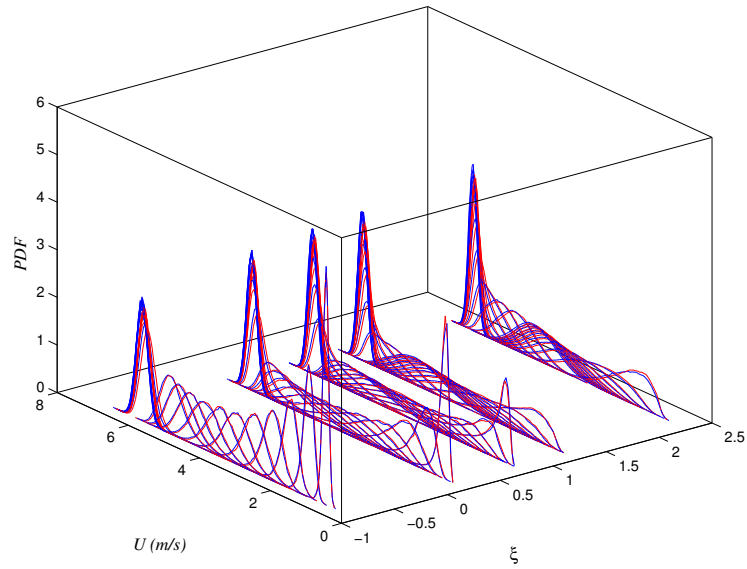


FIGURE 5.19. PDF distribution in streamwise (ξ) and wall-normal directions. Different colors show two different hot wires.

Spanwise measurements inside the transitional boundary layer

Spanwise measurements were done at five different streamwise distances from the leading edge and at the location above the wall of maximum u_{rms} . These measurements have been carried out at minimum and maximum injection when the grid was located at the closest and farthest downstream distances from the leading edge.

6.1. Mean velocity and the higher order moments including intermittency

The measurements were carried out at 20 points within 17 mm in the spanwise direction. As shown in figure 6.1, all velocity moments are almost constant along z but with some scatter. The small slope of the data; which can be observed in figure 6.1 (a) is because of the fact that the z traversing system was not completely parallel to the plate.

Besides the mean velocity and higher order moments, the intermittency of the velocity signal can be calculated in the spanwise direction. For a better view, the result is presented in a 3D plot. The non-dimensional x coordinate (ξ) and z correspond to the two axes. Figure 6.2 depicts such a graph and shows very nicely the two-dimensionality of the transition region when statistically presented.

The same as 6.1, it is clear that the intermittency does not change in the spanwise direction. In addition by looking at 2D (γ vs. ξ) the trend looks the same as in figure 4.6.

6.2. Two-point spanwise correlation

The spanwise correlation (R_{uu}) can be obtained from two-hot wire signals acquired simultaneously at different distance from each other. The two-point spanwise correlation function has been used extensively in FST transitional boundary layers in order to say some thing about the spanwise length scale of the disturbance structures. The spanwise distance (Δz) between the two hot-wires where a negative minimum in $R_{uu}(\Delta z)$ appears may be interpreted as the averaged half spanwise wavelength of the streaky structures ($\lambda_z/2$).

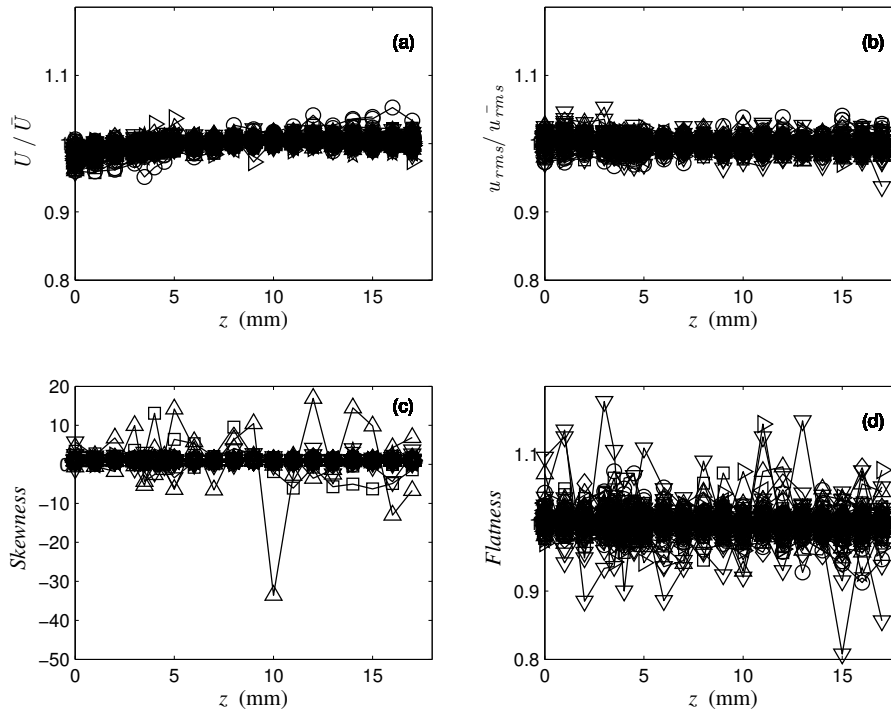


FIGURE 6.1. Normalized mean velocity and higher order moments along z . All the quantities are normalized by its averaged value.

In calculating the R_{uu} distribution in a highly intermittent boundary layer, naturally it will be difficult to find a negative correlation between the two hot-wires. Once the streaks have broken down into turbulence spots they will not exist any longer and hence a spanwise wavelength of the streaky structures will not be found. However, it is well-known that there exists near-wall streaks in turbulent boundary layer and hence for an increasing Reynolds number a spanwise wavelength is again expected to be found. When the boundary layer is contaminated by turbulent spots, they will destroy the possibility to find the negative distance in R_{uu} due to the fact that a spot is likely to pass both hotwires and hence a strong positive correlation contribution is obtained. A way to get around this problem is to systematically remove portions of the hot-wire signals where turbulent spots appear and to perform the spanwise correlation on the restoring uncontaminated signals. The filtering technique, which was applied here, is described in below subsection.

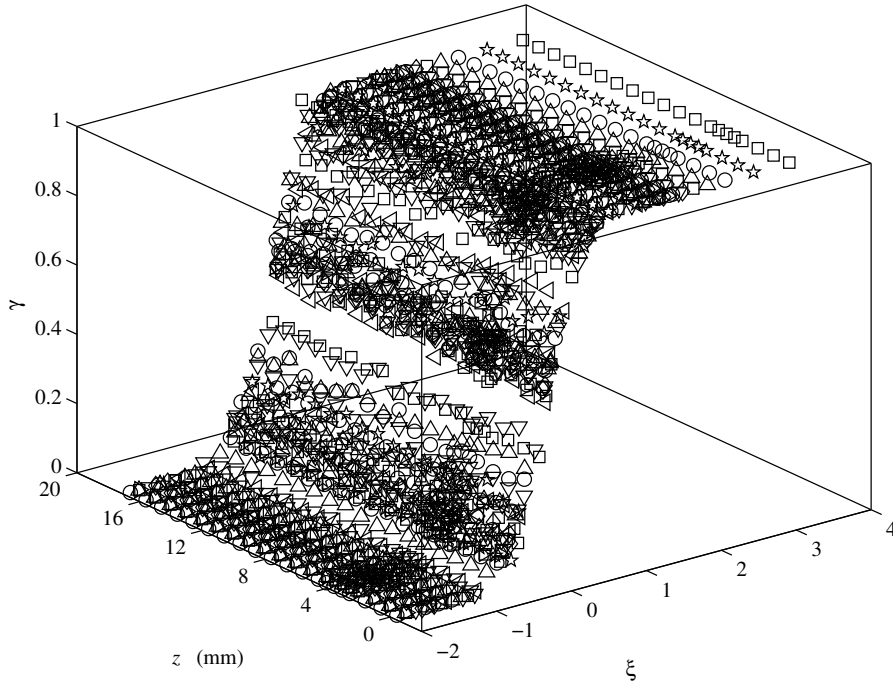


FIGURE 6.2. Intermittency evolution in the streamwise and spanwise directions.

6.2.1. Filtering technique

First of all, in the transition region when a turbulent spot passes both sensors the correlation between the hot-wires destroys (see e.g. Yoshioka *et al.* 2004). So, the signal lengths which are affected by the spots should be subtracted from the original signal. It should be mentioned that this subtraction is done at the same time on both signals. The procedure is almost the same as explained the method for calculating intermittency. The cut-off low-pass frequency and threshold were chosen as $f_{cut} = 250$ Hz and $u_{rms}^2 < 3 \times 10^{-4}$ respectively. On the other hand, by increasing the intermittency the so-called clean signals which can be obtained decrease and in some cases even if the filtering has been applied the correlation never reach a negative number. In these cases the correlation is neglected.

In addition, although it was tried that the hot-wires to be really close to each other, there is a distance between them in reality. Therefore, we can not measure the correlation at $\Delta z = 0$ mm. By the fact that the correlation and it's gradient at $\Delta z = 0$ mm are equal to zero and fit a second order curve, the real distance between the hot-wires at the first point can be measured.

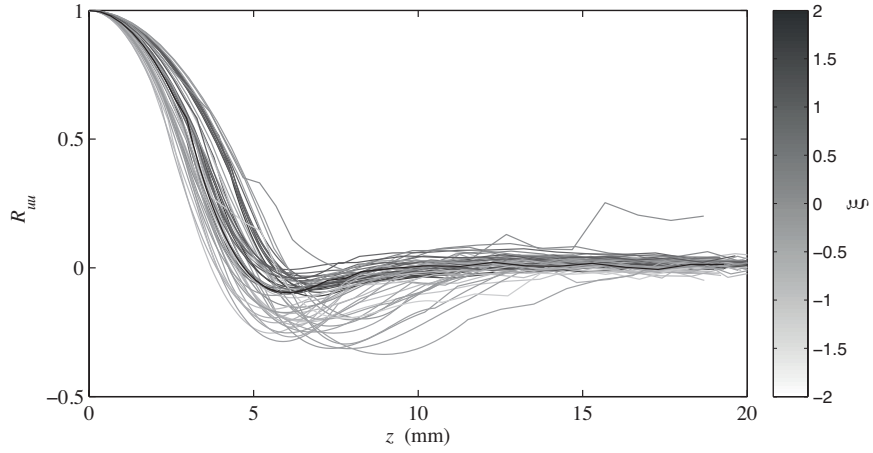


FIGURE 6.3. Spanwise correlation of two hot wire. The color bar shows the non-dimension x (ξ).

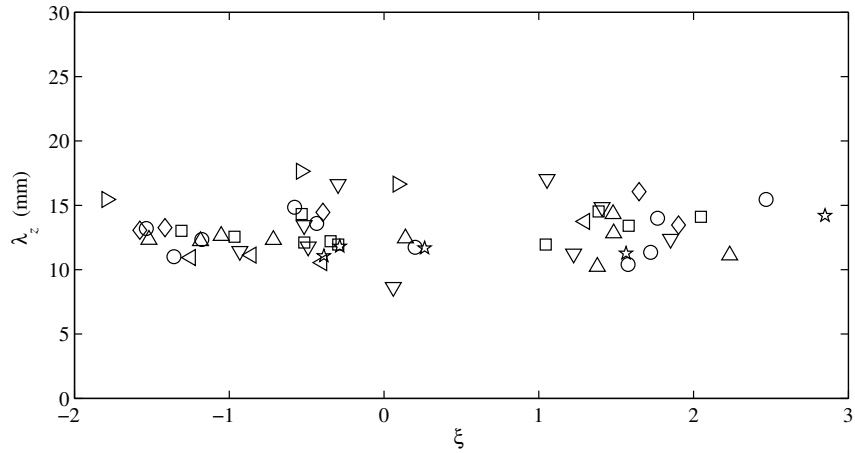


FIGURE 6.4. Spanwise wavelength in different ξ . It seems that the wavelength does not change much, but in some cases increases little. Different symbols show different grids.

Furthermore, for capturing the location of minimum correlation (which correspond to half the wavelength in the spanwise direction), a third order polynomial fit was applied on the data in the region near the minimum.

In figure 6.3 all the two-point spanwise correlation functions are shown after having applied the filtering on the signals and treated the R_{uu} when $\Delta z \rightarrow 0$ as described above. The minimum negative values have been determined for

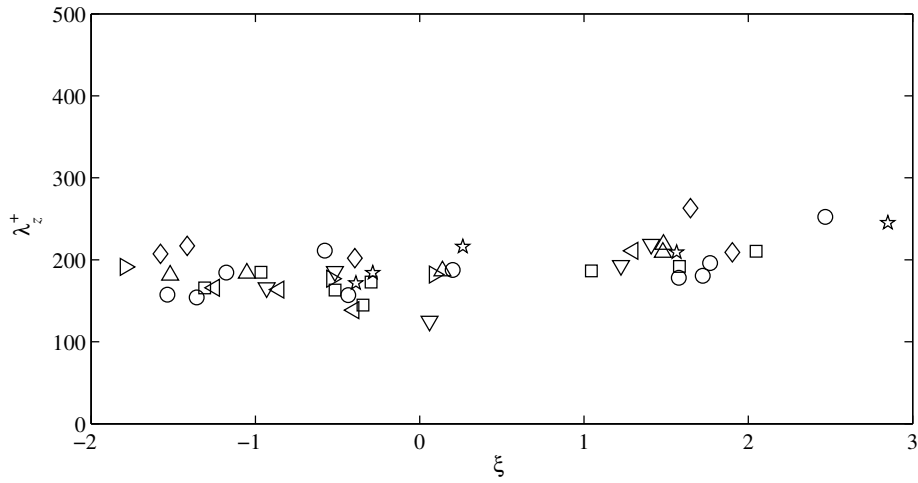


FIGURE 6.5. Scaled spanwise wavelength in different ξ . The spanwise wavelength λ_z is normalized by l^* .

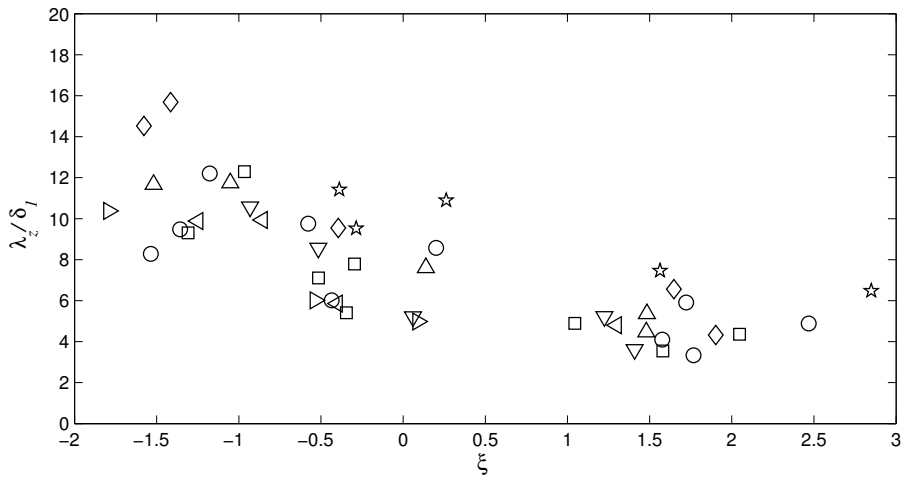


FIGURE 6.6. Scaled spanwise wavelength in different ξ . The spanwise wavelength λ_z is normalized by δ_1 .

each R_{uu} by fitting a 3rd order polynomial in three points in each side of the measured minimum and then taking the minimum values in this polynomial. Figure 6.4 shows the result, where the averaged half spanwise wavelength is plotted for each case, where the spanwise traverse were done. Although in some cases a slight increasing trend can be observed, the whole view reveals

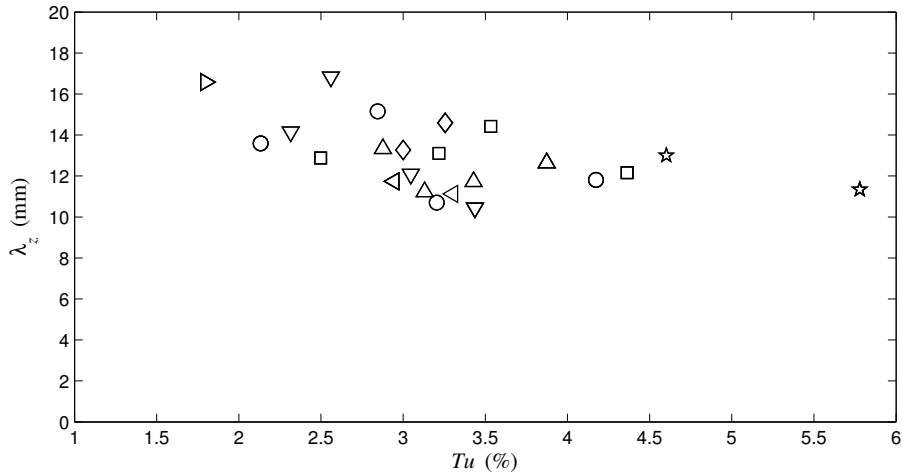


FIGURE 6.7. A decreasing trend for spanwise wavelength λ_z when Tu increases at the leading edge.

a constant spanwise wavelength. The gap in the range of $0.1 < \xi < 1.0$ corresponds to neglected signals where the so-called clean signals were not available.

Figures 6.5 and 6.6 show the scaled spanwise wavelength by two quantities; inner length scale (l^*) and displacement thickness (δ_1). Because these quantities were calculated in different streamwise distance from the leading edge compared to spanwise measurements, an interpolation was done when the point is between minimum and maximum locations where wall normal measurements had done. In addition, when the point is before the first wall normal measurement (usually at the laminar region), the theoretical laminar relation were carried out to estimate l^+ and δ_1 . On the other hand, if the point is located after last point, the same value as the last point employed. The reason is that as is seen in figure 5.3, the flow is not completely turbulent. Therefore, the empirical turbulence relation shows a large deviation from the measured values. Again by figure 5.3, one can conclude that c_f (and therefore u_τ and l^*) is almost constant in transitional region. So, in figure 6.5, λ_z^+ does not change along x . But from figure 5.2, it is clear that δ_1 increases as \sqrt{x} . Therefore, the decrease in λ_z/δ_1 is expected in figure 6.6.

Figures 6.7, 6.8 and 6.9 show the streamwise average of spanwise wavelength inside the boundary layer as a function of turbulence intensity (Tu), integral length scale (Λ_x) and Taylor length scale (τ), respectively, all at the leading edge. Although it seems that spanwise wavelength is independent of Λ_x and τ , there is a decreasing trend versus turbulence intensity (Tu) at the leading edge.

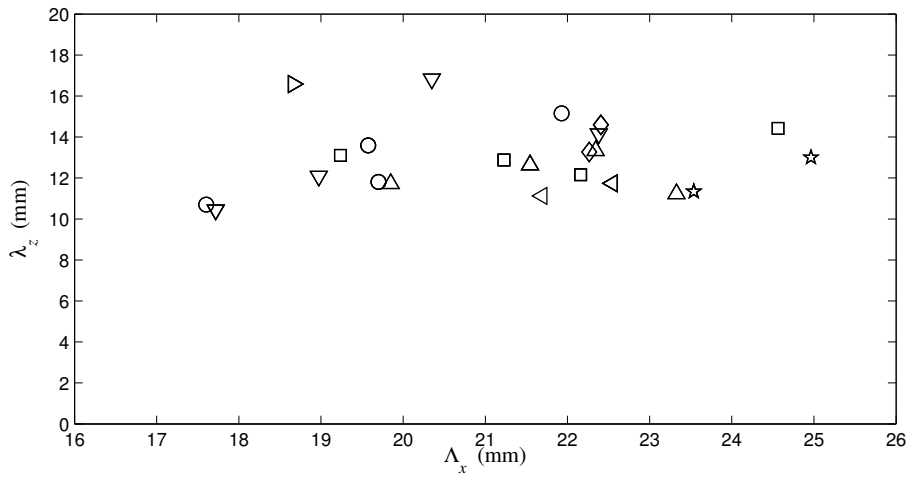


FIGURE 6.8. It seems that the integral length scale (Λ_x) at the leading edge does not have any influence on the spanwise wave length (λ_z) .

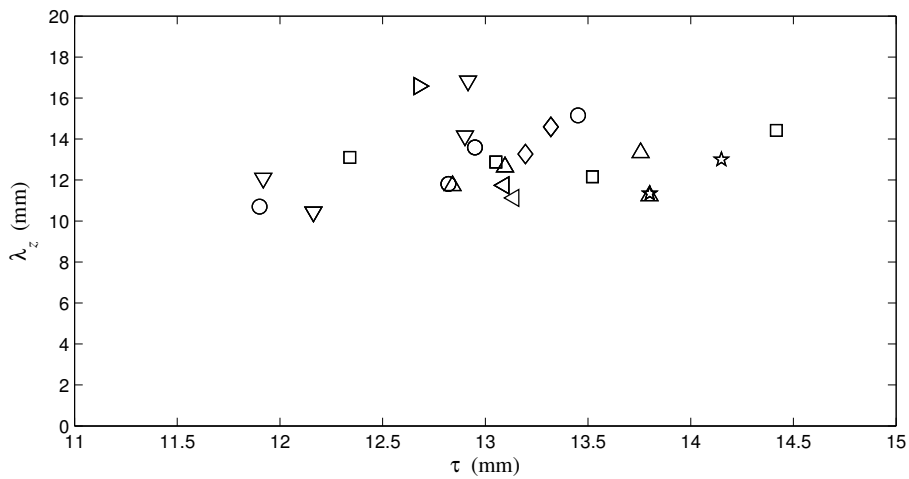


FIGURE 6.9. It seems that the Taylor length scale (τ) at the leading edge does not have any influence on the spanwise wave length (λ_z) .

Beside the location of minimum correlation, the closest position where the correlation is equal to zero can be calculated. Figure 6.10 shows the ratio between the locations of minimum and first zero correlation ($c = z_{min}/z_0$).

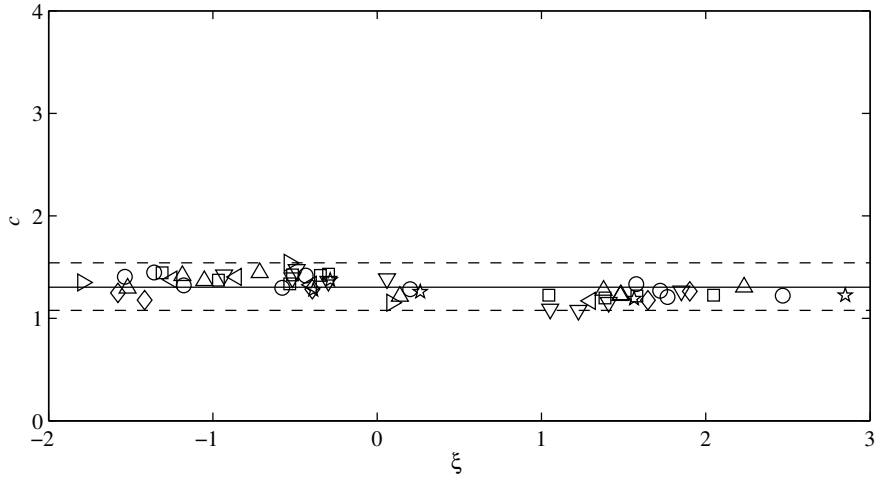


FIGURE 6.10. The ratio between the locations of minimum and first zero correlation ($c = z_{min}/z_0$). Different symbols show different grids.

Although as observed all the values collapse on the average of 1.30 with a tolerance of ± 0.23 , this ratio has a value over and below the average for laminar and turbulent region respectively. Fransson & Alfredsson (2003) did the same and reported $c = 1.68 \pm 0.23$. The difference can be because of the differences between the cases and the most important one is the free-stream velocity: where in this investigation $U_\infty = 6$ m/s, Fransson & Alfredsson (2003) locked the free stream velocity at $U_\infty = 5$ m/s. So, the higher free-stream velocity can be lead to the sharper curvature and therefore lower ratio of c .

CHAPTER 7

Summary and conclusions

The hot-wire anemometry technique was employed to investigate the transitional boundary layer in presence of free-stream turbulence (FST). Previous studies have indicated that it is not only the turbulence intensity (Tu) which determines the transition location, but also the turbulence characteristic length scales. However, the statistical basis is too small and hence the influence of the FST length scales on the transition location has been inconclusive. In this investigation a parameter study has been performed by varying both the turbulence intensity and FST length scales. In order to reduce the number of influencing parameters on the receptivity process, the free-stream turbulence velocity was kept constant at 6 m/s in all experiments, and hence the boundary layer scale is the same in all experiments. The experimental setup was validated and the natural boundary layer developing without FST was close to the Blasius boundary layer. Six active grids (with the possibility of applying upstream air injection) and two passive grids were used to obtain many different FST characteristics. The measurements were carried out in three directions: spanwise, streamwise and in the wall-normal direction. The turbulence intermittency, higher order velocity moments and spanwise correlation curves were calculated. In the analyses of the present data, an objective method to determine the wall position was used. This method also gives an estimation of the wall shear stress, which in turn allows the data to be plotted in inner scaling and compared with the outer scaling. The most important results of this investigation are summarized below point-by-point.

- The intermittency and higher order velocity moments do not change in the spanwise direction and hence the transition in the spanwise direction may be considered as two-dimensional in a statistical sense, the setup is clean with a uniformly smooth plate in the spanwise direction without any spanwise preference of the flow to transition to turbulence.

- The turbulence intensities at the leading edge, generated with the new active grids, is a function of the pressure inside the grids and therefore the jet

velocity from the active grids. The higher the jet velocity is the higher turbulence intensity is obtained.

- The result by Fransson *et al.* (2005) of a universal intermittency distribution in the streamwise direction, using the non-dimensional coordinate ξ , is here reinforced by showing the universality even though the FST integral length scale spans from 15 to 25 mm, i.e. an increase of over 70%.

- The transition zone is proportional to the onset of transition and a minimum distance from the leading edge is required for the receptivity process to be completed, even for high Tu 's. It should be noted that the relative length of the transition zone increases with increasing turbulence intensity.

- The turbulence intensity is clearly the most important parameter for the transition location. In this investigation it is shown that the FST length scales have a weak but peculiar effect on the transition location. For low Tu levels, longer length scales advance transition, in agreement with previous investigations, but for high Tu levels, the result is the opposite as well as weaker.

- Higher order velocity moments vary dramatically in the transition region which can be connected to the streak formation and the break-down in to turbulent spots.

- In the early stage of the transition process, the intermittency distribution in the wall-normal direction is almost constant, which is in agreement with previous results. Later in the transition process, the intermittency increases with increasing wall distance.

- While the location of maximum energy inside the boundary layer moves towards the wall in the streamwise direction, there is maximum value at the end of the transition region, around $\gamma=90\%$. From this location of maximum energy, the energy will decrease and saturate to a constant value around $(u_{rms}/U_\infty)^2 = 0.012$ in the turbulent boundary layer.

- The spanwise wavelengths of the streaky structures do not seem to be affected by the FST length scales. On the other hand, there is a clear trend of decreasing wavelength with increasing Tu .

- The spanwise wavelength of the streaky structure is constant when scaled with the viscous length scale ($\lambda_z^+ \approx 200$), i.e. independent of both Tu and the FST length scales.

APPENDIX A

Objective method for calculating boundary layer parameters

Jens H. M. Fransson & Shahab Shahinfar

Authors contributions of appendix A: the curve fitting program which is described in the present appendix was developed by JF with the input from SS. The appendix was written by JF with feed-back from SS. The program has been used by SS in evaluating the wall-normal profiles in the present thesis.

In the following appendix an objective method for calculating boundary layer parameters and other quantities in a transitional boundary layer is described. The hot-wire measurement technique is considered to be the most accurate technique for velocity disturbance measurements but is associated with a number of drawbacks. In laminar or transitional boundary layers the main problems are: (i) the determination of the wall position relative to the probe, (ii) heat conduction to the wall, and (iii) natural convection from the sensing wire including calibration at low velocities. The first issue is the subject of the present appendix while the second is well documented and hence is not treated here. The last-mentioned, (iii), can be dealt with using the calibration function proposed in Johansson & Alfredsson (1982), where an extra term is added to the King's law for compensation of natural convection. This modified King's law,

$$U = k_1 (E^2 - E_0^2)^{1/n} + k_2 (E - E_0)^{1/2} ,$$

where $E = E_0$ is the output voltage from the anemometer at zero velocity ($U = 0$) and k_1 , k_2 and n are the calibration coefficients determined in a least square fit sense to the calibration data, is really suited for low speed experiments.

It is well known that the displacement thickness (δ_1) is more sensitive than the momentum thickness (δ_2) to inaccurate wall location determination. By assuming the wall-normal coordinate to take the inaccurate value of \hat{e} ($\neq 0$) at the wall an error estimation may be performed (see e.g. Fransson 2001, for such analysis). Below integrals,

$$\begin{aligned}\delta_1 &= \int_{\hat{\varepsilon}}^{\delta^*} \left(1 - \frac{U(y)}{U_\infty}\right) dy, \\ \delta_2 &= \int_{\hat{\varepsilon}}^{\delta^*} \left(1 - \frac{U(y)}{U_\infty}\right) \frac{U(y)}{U_\infty} dy,\end{aligned}$$

with the upper free-stream limit of the wall-normal coordinate truncated at δ^* , may be expanded by assuming a Blasius boundary layer profile (i.e. that the velocity is proportional to the wall-normal distance near the wall) and that $U(\hat{\varepsilon}) \ll U_\infty$. This leads to,

$$\begin{aligned}\delta_1 &\approx \delta_1^{\text{true}} - \hat{\varepsilon}, \\ \delta_2 &\approx \delta_2^{\text{true}},\end{aligned}$$

when considering a first order error expansion. For $\hat{\varepsilon} > 0$ the displacement thickness is underestimated by an equal amount while the momentum thickness is unchanged when considering a first order error expansion. This in turn results in an inaccurate shape factor H_{12} which is underestimated.

Above analysis emphasizes the importance of determining the wall location accurately if accurate boundary layer parameters are desired. This analysis is however not valid in a transitional boundary layer when the Blasius boundary layer has been modulated by the high amplitude disturbances. For low disturbance amplitudes the displacement thickness is hardly affected since the velocity excess in the inner region close to the wall is being compensated by the velocity deficit in the outer region of the boundary layer. A standard technique to estimate the wall location is to set up a clean base flow, which is free from external disturbance sources, and adjust the pressure gradient to comply with the Blasius boundary layer condition. Then the wall position can be estimated quite accurately by linearly extrapolating the wall-normal coordinate down to zero velocity at the wall. On the other hand as soon as the boundary layer is modulated by the disturbances, which is manifested by a fuller mean velocity profile close to the wall, a linear extrapolation would give erroneous wall locations and hence is no longer a recommended alternative. This issue was discussed by White & Ergin (2004), who performed a boundary layer transient disturbance growth investigation behind a periodic array of cylindrical roughness elements, which were equally spaced in the spanwise direction. Depending on the spanwise location the profile may be highly distorted with strong regions of velocity excess or velocity deficit, which gives rise to the problem of accurately determining the wall position. White & Ergin still used a linear curve fitting technique, locally, on the wall-normal velocity profiles but only on selected spanwise positions, which were judged not to be strongly influenced by the upstream roughness.

In this work a curve fitting technique has been developed in order to get a good estimation of the wall position given a wall-normal velocity profile. In

addition to the wall position one may get a good estimate of the wall shear stress by calculating the velocity gradient at the wall using the fitted profile. For low intermittency values (γ), i.e. $\gamma < 0.25$, a Falkner-Skan solver was used in the curve fitting procedure where the acceleration/deceleration parameter m , wall-normal location y_w and a stretching/squeezing parameter \mathcal{C} on the wall-normal coordinate were determined such that the error between the experimentally measured data and the general numerical solution to the boundary layer equation was minimized. The parameter \mathcal{C} can be seen as a correction for a virtual origin, but is usually close to unity. For higher intermittency values the Falkner-Skan solution fails to describe the mean velocity profile alone. On the other hand by using a composite profile for turbulent boundary layers (U_{CTBL}) together with the Falkner-Skan profile (U_{FS}), which are weighted by the single parameter \mathcal{A} as,

$$U_{\text{fit}} = (1 - \mathcal{A}) \cdot U_{\text{FS}} + \mathcal{A} \cdot U_{\text{CTBL}} , \quad (\text{A.1})$$

one may find a velocity profile U_{fit} with a small deviation from the experimental data points. Here, the composite profile by Nickels (2004) was used, which can be written out in its explicit form as

$$\begin{aligned} U_{\text{CTBL}}^+(y^+, \eta) = & y_c^+ [1 - (1 + 2(y^+/y_c^+) + \frac{1}{2}(3 - p_x^+ y_c^+)(y^+/y_c^+)^2 \\ & - \frac{3}{2} p_x^+ y_c^+ (y^+/y_c^+)^3) e^{-3y^+/y_c^+}] \\ & + \frac{\sqrt{1 + p_x^+ y_c^+}}{6\kappa_o} \ln \left(\frac{1 + (0.6(y^+/y_c^+))^6}{1 + \eta^6} \right) \\ & + b \left(1 - e^{-\frac{5(\eta^4 + \eta^8)}{1 + 5\eta^3}} \right) , \quad (\text{A.2}) \end{aligned}$$

where $\kappa_o = 0.39$ is the universal von Kármán constant, $y_c^+ = 12$ and $p_x^+ = 0$ for a zero pressure gradient turbulent boundary layer (cf. Nickels 2004). y^+ and η correspond to the wall-normal coordinate scaled with inner and outer length scales, respectively. In addition to m , y_w and \mathcal{C} there are three more parameters to be determined in the curve fit of U_{fit} in eq. (A.1). These are the weight factor \mathcal{A} , the skin-friction velocity u_τ and the coefficient b in the last term of eq. (A.2) corresponding to the wake function. For γ values greater than 0.9 eq. (A.2) is used alone reducing the number of parameters to be determined in the curve fit to four, since m and \mathcal{A} are no longer used. It should be mentioned that in this range of γ values the final curve fitted profile deviates from the experimentally measured profile in the outer region but still do a good job in the inner region. The reason for the worse curve fit is because of the relatively low Reynolds number in this late stage of the transition scenario. Even for γ values of one the fit is not satisfactory in this outer region due to the undeveloped turbulent boundary layer.

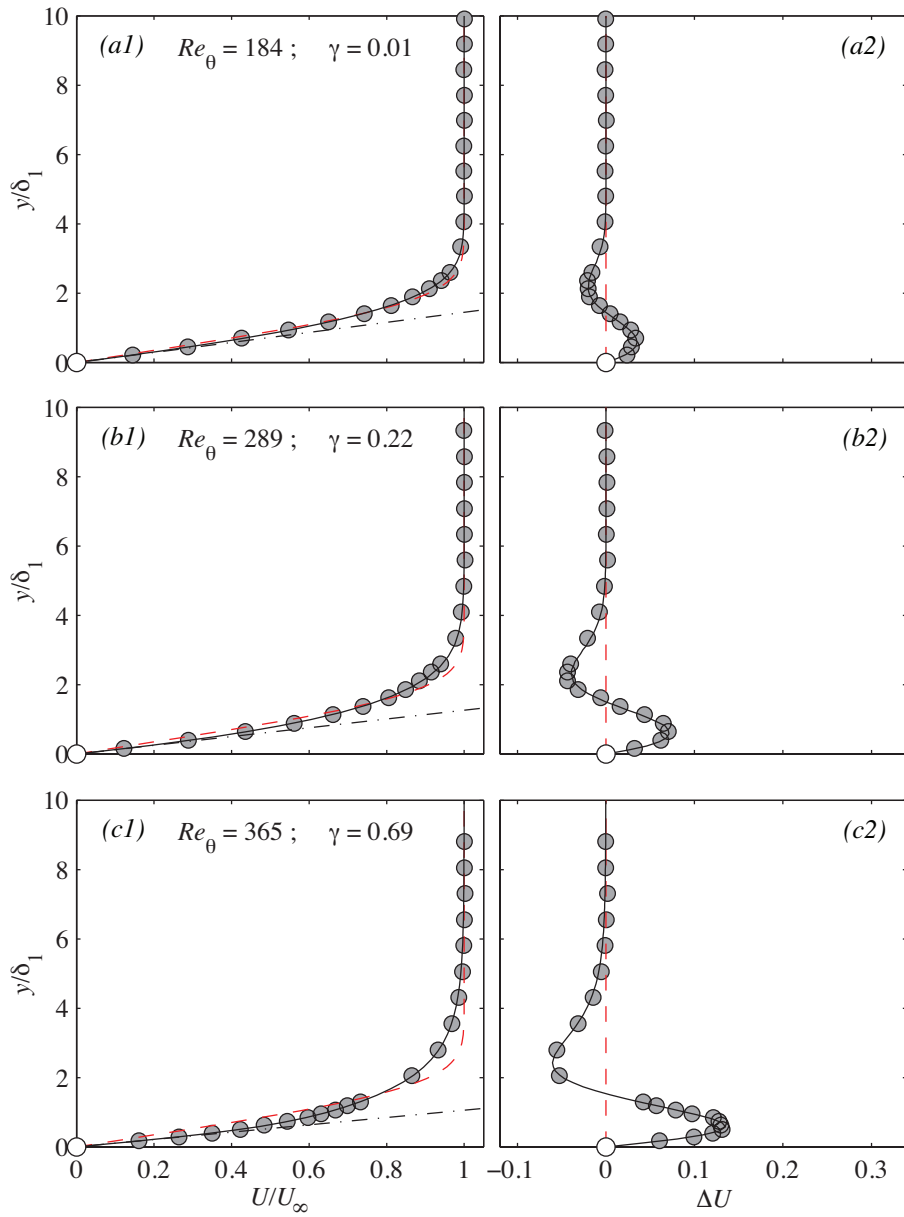
Above method is here applied on five mean velocity profiles in a transitional boundary layer subjected to free-stream turbulence (FST) in order to illustrate how this objective wall determination method works in practice. The FST characteristics at the leading edge of the chosen case is; turbulence intensity of 3.15%, integral length scale of 17.5 mm and Taylor length scale of 11.9 mm. It should be noted that the boundary layer integral length scales are an output from the developed curve fitting program, but have been calculated solely on the experimental data using a trapezoidal integration technique after having corrected for the wall position, i.e. the fitted mean velocity profile U_{FS} , U_{fit} or U_{CTBL} (depending on the γ value) are only used here for validation of the curve fitting procedure and in order to estimate the wall shear stress (τ_w). In figure A.1 left column (1) the wall-normal mean velocity profiles are shown for different γ values throughout the transition region. The right column (2) shows the deviation from the Blasius profile, i.e. $\Delta U = U_{fit} - U_{Blasius}$. Symbols correspond to the experimentally measured data points, the dashed line to the Blasius boundary layer profile and the solid line to the fitted profile. The dash-dotted line corresponds to the wall velocity gradient calculated, as described above, by using the near wall points from the fitted profile. The intermittency factor was here calculated using the same procedure as described in Fransson *et al.* (2005). The boundary layer integral length scales and the shape factor of the mean velocity profiles in figure A.1 are displayed in figure A.2(a). In figure A.2(b) the skin-friction coefficient (c_f) is shown for the five profiles. The skin-friction coefficient was here calculated as,

$$c_f \equiv \frac{\tau_w}{q_\infty} = \dots = \frac{2}{Re_{\delta_1}} \left[\frac{d(U/U_\infty)}{d(y/\delta_1)} \right]_{y=0}, \quad (\text{A.3})$$

where q_∞ and Re_{δ_1} are the dynamic pressure and the Reynolds number based on the displacement thickness, respectively.

In summary, a curve fitting program has been developed in order to determine the wall position, in a transitional boundary layer, in an accurate and objective way. Having determined the wall position the integral length scales, describing the boundary layer evolution, may be calculated with confidence. The method uses the numerical solution to a laminar boundary layer with arbitrary pressure gradient, the so called Falkner-Skan boundary layer profile, in order to capture small deviations from the Blasius boundary layer in the pre-transitional region. In the transitional region this method fails to describe the profile if used alone, here, we have made use of an existing turbulent composite profile in combination with the Falkner-Skan profile using a weighting factor on their respective contributions. In the post-transitional region the composite profile is used alone. The program is robust since it uses initial conditions based on the experimental input profile, which always leads to a converged iterative solution. Finally, the fitted profile may be used to estimate the wall shear stress in an objective way, which is a quantity often extracted from mean

velocity data even though there is a lack of near wall data points and hence most likely associated with a high degree of uncertainty.



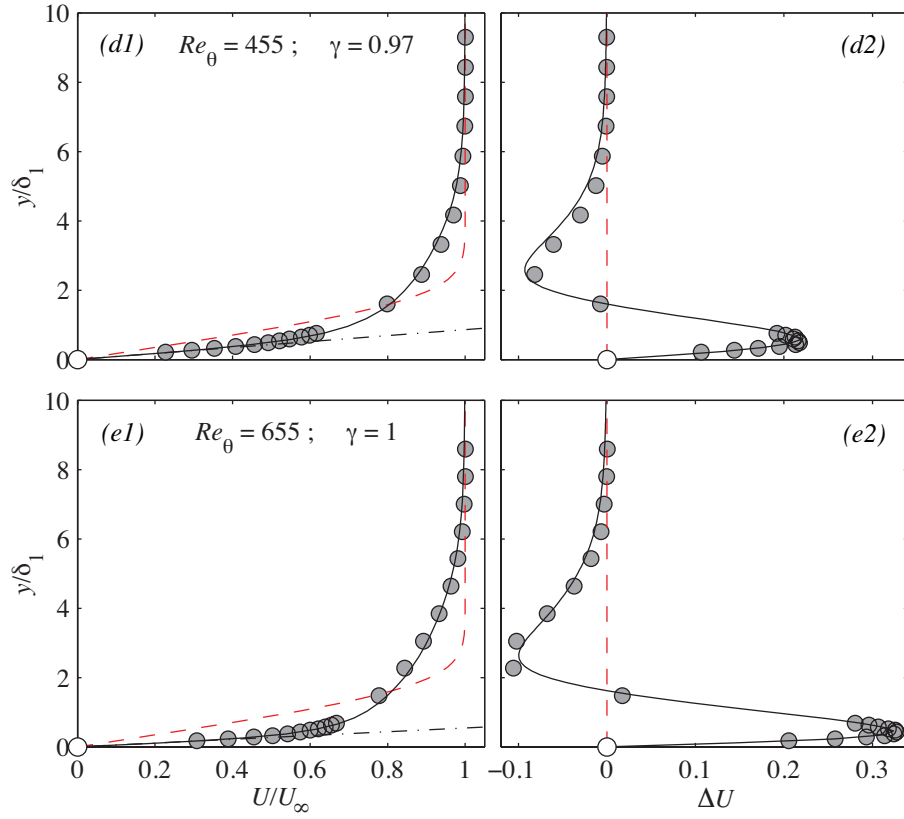


FIGURE A.1. Wall-normal mean velocity profiles (left column) and its deviation from Blasius (right column). Symbols correspond to experimental data, dashed line to the Blasius profile, solid line to the fitted profile and dash-dotted to the wall velocity gradient. (a)–(e) is shown for successively increasing intermittency factor (γ) and Reynolds number (Re_θ).

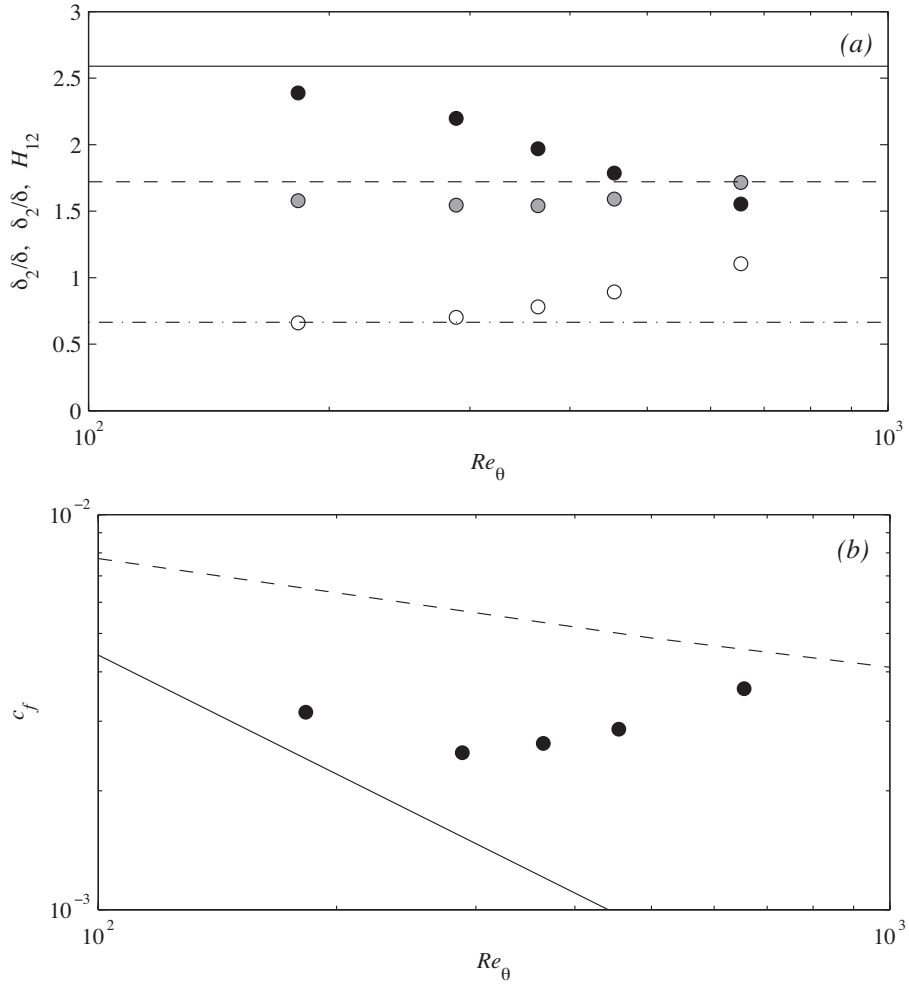


FIGURE A.2. Figure (a) shows the evolution of the displacement thickness (δ_1 gray symbols), the momentum thickness (δ_2 white symbols) and their ratio (H_{12} black symbols) for successively increasing Reynolds number. The dashed, dash-dotted, and solid lines correspond to the Blasius solution of above mentioned quantities, respectively. Figure (b) shows the evolution of the skin-friction coefficient with the solid line corresponding to the Blasius solution and the dashed line to a semi-empirical skin-friction relation for fully developed turbulent boundary layers, $c_f = 2 [1/\kappa \cdot \log(Re_\theta) + \mathcal{B}]^{-2}$.

Acknowledgements

First of all, it is my responsibility to thank Docent Jens Fransson and Prof. Henrik Alfredsson for trusting me to continue my education as a graduate student in KTH and have supported me since I started.

I also would like to thank Dr. Ramis Örlü and Dr. Thomas Kurian to share their knowledge to help me to learn more about the subject and perform the experiments better. Special thanks to Joakim Karlström and Göran Rådberg, not only for the perfect manufacturing, but also for the tactful suggestions and designs.

The investigation could not be performed without a nice and calm atmosphere next to my office mates Bengt and Malte.

Here, I should apologize all sitting in hall 49 for long noisy experiments (c.f. section 3.1) in summer 2010.

The financial support by the Linné Flow Center is gratefully acknowledged.

References

- ANDERSSON, P., BERGGREN, M. & HENNINGSON, D. S. 1999 Optimal disturbances and bypass transition in boundary layers. *Phys. Fluids* **11**, 134–150.
- ARNAL, D. & JUILLEN, J. C. 1978 Contribution expérimentale à l'étude de la receptivité d'une couche limite laminaire, à la turbulence de l'écoulement general. Rapport Technique 1/5018 AYD. ONERA.
- BATCHELOR, G. K. & TOWNSEND, A. A. 1948 Decay of isotropic turbulence in the initial period. *Proc. R. Soc. Lond A* **193**, 539–558.
- BRANDT, L., SCHLATTER, P. & HENNINGSON, D. 2004 Transition in boundary layers subject to free-stream turbulence. *J. Fluid Mech.* **517**, 167–198.
- FRANSSON, J. H. M. 2001 Investigations of the asymptotic suction boundary layer. TRITA-MEK Tech. Rep. 2001:11. KTH, Stockholm, licentiate Thesis.
- FRANSSON, J. H. M. 2004 Leading edge design process using a commercial flow solver. *Experimental in Fluid* **37**, 929–932.
- FRANSSON, J. H. M. & ALFREDSSON, P. H. 2003 On the disturbance growth in an asymptotic suction boundary layer. *J. Fluid Mech.* **482**, 51–90, **Paper 1**.
- FRANSSON, J. H. M., MATSUBARA, M. & ALFREDSSON, P. H. 2005 Transition induced by free stream turbulence. *J. Fluid Mech.* **527**, 1–25.
- GAD-EL-HAK, M. & CORRSIN, S. 1974 Measurements of the nearly isotropic turbulence behind a uniform jet grid. *J. Fluid Mech.* **62**, 115–143.
- JOHANSON, M. W. & FASHIFAR, A. 1994 Statistical properties of turbulent bursts in transitional boundary layer. *Int. J. Heat Fluid Flow* **15**, 283–290.
- JOHANSSON, A. V. & ALFREDSSON, P. H. 1982 On the structure of turbulent channel flow. *J. Fluid Mech.* **122**, 295–314.
- JONAS, P., MAZUR, O. & URUBA, V. 2000 On the receptivity of the by-pass transition to the length scale of the outer stream turbulence. *Eur. J. Mech.* **B19**, 707–722.
- KENDALL, J. M. 1985 Experimental study of disturbances produced in a pre-transitional laminar boundary layer by weak free stream turbulence. *AIAA Paper* **85-1695**.
- KLEBANOFF, P. S. 1971 Effect of freestream turbulence on the laminar boundary layer. *Bull. Am. Phys. Soc.* **10**, 1323.
- KLINGMANN, R. G. B., BOIKO, A. V., WESTIN, K. J. A., KOZLOV, V. V. &

- ALFREDSSON, P. H. 1993 Experiments on the stability of Tollmien-Schlichting waves. *Eur. J. Mech., B/Fluids* **12**, 493–514.
- KURIAN, T. & FRANSSON, J. H. M. 2009 Grid generated turbulence revisited. *Fluid Dynamics Research* **41** 021403.
- LANDAHL, M. T. 1980 A note on an algebraic instability of inviscid parallel shear flows. *J. Fluid Mech.* **98**, 243–251.
- LINDGREN, B. & JOHANSSON, A. V. 2002 Design and evaluation of a low-speed wind-tunnel with expanding corners. TRITA-MEK Tech. Rep. 2002:14. KTH, Stockholm.
- MATSUBARA, M. & ALFREDSSON, P. H. 2001 Disturbance growth in boundary layers subjected to free-stream turbulence. *J. Fluid Mech.* **430**, 149–168.
- MORKOVIN, M. V. 1969 *The many faces of transition*. In *Viscous Drag Reduction*, Plenum Press.
- NAGARAJAN, S., LELE, S. K. & FERZIGER, J. H. 2007 Leading-edge effects in bypass transition. *J. Fluid Mech.* **572**, 471–504.
- NICKELS, T. B. 2004 Inner scaling for wall-bounded flows subjected to large pressure gradients. *J. Fluid Mech.* **521**, 217–239.
- OVCHINNIKOV, V. O., PIOMELLI, U. & CHOUDHARI, M. M. 2004 Inflow conditions for numerical simulations of bypass transition. *AIAA* p. 0591.
- TAYLOR, G. I. 1939 Some recent developments in the study of turbulence. In *Proc. Fifth Int. Cong. Appl. Mech., 12-16 September 1938* (ed. J. P. den Hartog & H. Peters), pp. 294–310. Cambridge, MA, USA: Wiley.
- WESTIN, J. 1997 Laminar-turbulent boundary layer transition influenced by free stream turbulence. PhD thesis, KTH, Stockholm, TRITA-MEK Tech. Rep. 1997:10.
- WESTIN, K. J. A., BAKCHINOV, A. A., KOZLOV, V. V. & ALFREDSSON, P. H. 1998 Experiments on localized disturbances in a flat plate boundary layer. part 1. receptivity and evolution of a localized free stream turbulence. *Eur. J. Mech. B/Fluids* **17**, 823–846.
- WESTIN, K. J. A., BOIKO, A. V., B. G. B. KLINGMANN, V. V. K. & ALFREDSSON, P. H. 1994 Experiments in a boundary layer subjected to freestream turbulence. part i. boundary layer structure and receptivity. *J. Fluid Mech.* **281**, 193–218.
- WHITE, E. B. & ERGIN, F. G. 2004 Using laminar-flow velocity profiles to locate the wall behind roughness elements. *Exp. in Fluids* **36**, 805–812.
- YOSHIOKA, S., FRANSSON, J. H. M. & ALFREDSSON, P. H. 2004 Free stream turbulence induced disturbances in boundary layers with wall suction. *Phys. Fluids* **16**, 3530–3539.